ATLAS NOTE

ATLAS-CONF-2013-068

July 17, 2013

Search for pair-produced top squarks decaying into charm quarks and the lightest neutralinos using 20.3 fb^{-1} of pp collisions at $\sqrt{s} = 8$ TeV with the ATLAS detector at the LHC

ATLAS Collaboration

Abstract

This note presents the search for direct top squark pair production in the decay channel to a charm quark and the lightest neutralino ($\tilde{t} \to c + \tilde{\chi}_1^0$), using 20.3 fb^{-1} of proton-proton collision data at $\sqrt{s} = 8$ TeV recorded by the ATLAS experiment at the LHC in 2012. The analysis is carried out in different signal regions according to the final state jet multiplicity. One of the regions uses charm-flavour identification to increase the signal purity. No excess above the Standard Model background expectation is observed. Limits are set on the visible cross-section of new physics within the requirements of the search. The results are interpreted in the context of direct pair production of top squarks and presented in terms of exclusion limits in the ($m_{\tilde{t}}$, $m_{\tilde{\chi}_1^0}$) plane. A top squark mass of 200 GeV is excluded at 95% confidence level for $m_{\tilde{t}}$–$m_{\tilde{\chi}_1^0} < 85$ GeV. Top squark masses up to 230 GeV are excluded for a neutralino mass of 200 GeV. This extends significantly previous Tevatron results.

ATLAS-CONF-2013-068
18 July 2013

1 Introduction

Supersymmetry (SUSY) [1–9] is a theoretically favoured candidate for physics beyond the Standard Model (SM). It naturally solves the hierarchy problem and provides a possible candidate for dark matter in the universe. SUSY doubles the SM spectrum of particles by introducing a new supersymmetric partner (sparticle) for each particle in the SM. In particular, a new scalar field is associated with each left- and right-handed quark state, and two squark mass eigenstates $\tilde{q}_1$ and $\tilde{q}_2$ result from the mixing of the scalar fields. In some SUSY scenarios, a significant mass difference between eigenstates in the top squark (stop) sector can occur, leading to a rather light stop $\tilde{t}_1$ mass state. In addition, naturalness arguments suggest that the third generation sfermions should be light with masses below 1 TeV. In a generic minimal supersymmetric extension of the SM (MSSM) that assumes R-parity conservation, sparticles are produced in pairs and the lightest supersymmetric particle (LSP) is stable and identified as the lightest neutralino $\tilde{\chi}_1^0$.

For a mass difference $\Delta m = m_{\tilde{t}} - m_{\tilde{\chi}_1^0} > m_t$, and depending on the SUSY parameters and mass hierarchy, the dominant decay channels are $\tilde{t} \to t + \tilde{\chi}_1^0$ or $\tilde{t} \to b + \tilde{\chi}_1^{\pm}$, where the latter involves the presence of charginos ($\tilde{\chi}_1^{\pm}$) which subsequently decay into the lightest neutralino via a $W^{(*)}$ emission. If the chargino is heavier than the stop and $m_W + m_b < \Delta m < m_t$, the dominant decay mode is expected to be the three-body $Wb\tilde{\chi}_1^0$ decay. Several searches on 2011 data have been carried out in these decay channels in 0 to 2 lepton final states [10–12] and have been extended in 2012 [13–16]. In the scenario for which $\Delta m < m_W + m_b$, the dominant decay mode can be a stop decay to a charm quark and the LSP ($\tilde{t} \to c + \tilde{\chi}_1^0$), which proceeds via a loop decay (see Fig. 1). The corresponding final state is characterized by the presence of two jets from the hadronization of the charm quarks and missing transverse momentum (denoting its magnitude by $E_{\mathrm{T}}^{\mathrm{miss}}$) from the two undetected LSPs. However, given the relatively small mass difference (Δm), both the transverse momenta of the two charm jets and the $E_{\mathrm{T}}^{\mathrm{miss}}$ are too low to extract this signal from the large multijet background.

In this study, the event selection makes use of the presence of initial-state radiation (ISR) jets to identify signal events. Two different approaches are used to target the different Δm regions. For small Δm,

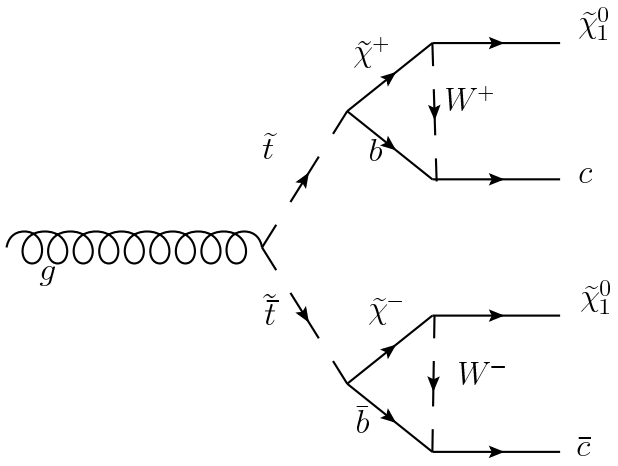

Figure 1: Feynman diagram for the pair production of top squarks with subsequent decay to charm quarks and two LSP's.

the approach follows closely the "monojet" analysis of Ref. [17], where events with low jet multiplicity and large missing transverse momentum are selected. For moderate Δm the charm jets receive a large enough boost to be detected. In addition to the requirements on the presence of ISR jets, charm tagging

is used, for the first time at the LHC, to enhance the SUSY signal. Results on searches in this channel using Tevatron data have been previously reported by both the CDF and D0 experiments [18, 19].

2 Monte Carlo simulation

Monte Carlo (MC) simulation samples are used to aid in the description of the background and to model the stop signal. The MC samples are processed either with a full ATLAS detector simulation [20] based on the Geant4 program [21] or a fast simulation based on the parameterization of the response of the electromagnetic and hadronic showers in the ATLAS calorimeters [22]. The effect of multiple pp interactions in the same or nearby bunch crossing is also simulated.

The `Sherpa` [23] generator is used to simulate W+jets and Z/γ^*+jets processes, assuming massive b/c-quarks, and the `Alpgen` [24] generator is employed to assess the corresponding modelling uncertainties. Production of top quark pairs is simulated with `Powheg` [25]. The `Alpgen` and `MC@NLO` [26] generators are used to assess the $t\bar{t}$ modelling uncertainty. Single top samples are generated with `MC@NLO` for the s– and Wt–channel while `AcerMC` [27] is used for single top production in the t–channel. Finally, $t\bar{t}$ samples with additional vector bosons are generated with `Madgraph` [28]. A top quark mass of 172.5 GeV is used consistently. Diboson samples (WW, WZ and ZZ production) are generated using `Sherpa`. Additional samples are generated with `Herwig` [29] to assess uncertainties. In case of `Powheg` and `Madgraph`, parton showers are implemented using `Pythia` [30, 31], and `Herwig` plus `Jimmy` [32] is used for the `Alpgen` and `MC@NLO` generators. The multijet background is determined from the data. For cross checks, dijet samples are generated with `Pythia`.

The cross sections for Z/γ^*, W and $t\bar{t}$ production at $\sqrt{s} = 8\,\text{TeV}$ are known at (approximate) next-to-next-to-leading order (NNLO) in perturbative QCD (pQCD): the values are $1.12 \pm 0.04\,\text{nb}$, $12.19 \pm 0.52\,\text{nb}$ and $238^{+22}_{-24}\,\text{pb}$, for $Z/\gamma^*(\to \ell\ell)$, $W \to (\ell\nu)$ and $t\bar{t}$, respectively. The Z/γ^* and W cross sections have been calculated with DYNNLO [33, 34] using MSTW2008 90% NNLO parton density function (PDF) sets [35]. The cross section for top pair production is calculated with Hathor 1.2 [36] using the MSTW2008 90% NNLO PDF sets incorporating PDF+α_S uncertainties, according to the MSTW prescription [37]. This is added in quadrature to the scale uncertainty and cross checked with the NLO+NNLL calculation [38] as implemented in Top++ 1.0 [39]. The single top cross sections are $5.6 \pm 0.2\,\text{pb}$ [40], $87.8^{+3.4}_{-1.9}\,\text{pb}$ [41] and $22.4 \pm 1.5\,\text{pb}$ [42] for the s-channel, t-channel and Wt-channel, respectively. Finally, the cross sections for top pair production in association with a W or Z boson are known at NLO precision and are $0.231 \pm 0.046\,\text{pb}$ and $0.206 \pm 0.021\,\text{pb}$ for $t\bar{t}W$ and $t\bar{t}Z$, respectively [43]. For WW, WZ, and ZZ production, NLO cross sections of $57.3^{+2.3}_{-1.6}\,\text{pb}$, $21.5^{+1,1}_{-0.9}\,\text{pb}$, and $7.92^{+0.37}_{-0.24}\,\text{pb}$ [44], respectively, are used.

Stop pair production with $\tilde{t} \to c + \tilde{\chi}^0_1$ is modelled with `Madgraph` with one additional jet from the matrix element. The showering is done with `Pythia`. Stop masses are produced between 100 GeV and 300 GeV in steps of 25 GeV and between 300 GeV and 400 GeV in steps of 50 GeV. $\tilde{\chi}^0_1$ masses are produced between 70 GeV and 390 GeV with a minimum mass difference of 5 GeV. The Δm step size increases with Δm from 5 GeV to 30 GeV. Signal cross sections are calculated to NLO in pQCD, adding the resummation of soft gluon emission at next-to-leading-logarithmic (NLO+NLL) accuracy [45–47]. The nominal cross section and the uncertainty are taken from an envelope of cross section predictions using different PDF sets and factorization and renormalization scales, as described in Ref. [48].

3 Reconstruction of physics objects

Jets are reconstructed from energy deposits in calorimeters using the anti-k_t jet algorithm [49] with the distance parameter (in $\eta - \phi$ space) [1] set to $R = \sqrt{\Delta\eta^2 + \Delta\phi^2} = 0.4$. The measured jet transverse momentum (p_{T}) is corrected for detector effects, including the non-compensating character of the calorimeter, by reweighting differently energy deposits arising from electromagnetic and hadronic showers. In addition, jets are corrected for contributions from multiple proton-proton interactions per beam bunch crossing (pileup), as described in Ref. [50]. $E_{\mathrm{T}}^{\mathrm{miss}}$ is reconstructed using all energy deposits in the calorimeter up to a pseudorapidity $|\eta|$ of 4.9. These clusters are calibrated taking into account the difference in response of jets compared to electrons or photons, as well as dead material and out-of-cluster energy losses [51]. Electron candidates are required to have $p_{\mathrm{T}} > 20$ GeV and $|\eta| < 2.47$, and to pass the *medium* electron shower shape and track selection criteria described in Ref. [52] and reoptimized for 2012 data. Muon candidates are required to have $p_{\mathrm{T}} > 10$ GeV and $|\eta| < 2.5$ and to pass the *combined* reconstruction criteria described in Ref. [53–55], which include the association of a stand-alone muon spectrometer track to an inner detector track. Overlaps between identified leptons and jets in the final state are resolved. Jets are discarded if their distance ΔR to an identified electron is less than 0.2. For the remaining jets in the events the electrons between 0.2 and 0.4 from a jet are removed. Similarly, muons are required to have $\Delta R > 0.4$ with respect to any selected jet in the event. In addition, as discussed below, the leptons used to veto events in the signal regions or to define control regions in data are required to be isolated. In the case of electrons, the total transverse momentum not associated with the electron in a cone of radius 0.2 around the electron candidate must be less than 10% of the electron's transverse momentum. For the muons, the sum of the transverse momenta of the tracks not associated with the muon is required to be less than 1.8 GeV.

3.1 Charm tagging

Jets are identified as originating from the hadronization of a charm quark (c-tagging) via a dedicated algorithm using multivariate techniques to combine information from the impact parameters of displaced tracks and topological properties of secondary and tertiary decay vertices reconstructed within the jet. The algorithm provides three weights, one targeted for light-flavor quarks and gluon jets (P_u), one for charm jets (P_c) and one for b-jets (P_b). From these weights, anti-b and anti-u discriminators are calculated (see Fig. 2):

$$\text{anti-}b \equiv \log\left(\frac{P_c}{P_b}\right) \qquad \text{and} \qquad \text{anti-}u \equiv \log\left(\frac{P_c}{P_u}\right),$$

and applied to the selected jets in the final state. Two operating points specific to c-tagging are used. The *medium* operating point ($\log\left(\frac{P_c}{P_b}\right) > -1$, $\log\left(\frac{P_c}{P_u}\right) > -0.82$) has a c-tagging efficiency of $\approx$ 20%, and a rejection factor of $\approx$ 5 for b-jets, $\approx$ 140 for light-flavor jets, and $\approx$ 10 for tau-jets. The *loose* operating point ($\log\left(\frac{P_c}{P_b}\right) > -1$) has a c-tagging efficiency of $\approx$ 95%, with a factor of 2 rejection of b-jets but without any significant rejection of light-flavor or tau jets. The efficiencies and rejections are quoted for simulated $t\bar{t}$ events for jets with $30\,\mathrm{GeV} < p_{\mathrm{T}} < 200\,\mathrm{GeV}$ and $|\eta| < 2.5$. The c-tagging efficiency is calibrated using data and the method described in Ref. [56]. The same method applied to the 8 TeV data leads to reduced uncertainties. The standard calibration techniques are used for the b-jet [57] and light-jet [58] rejections.

[1] ATLAS uses a right-handed coordinate system with its origin at the nominal interaction point (IP) in the centre of the detector and the z-axis along the beam pipe. The x-axis points from the IP to the centre of the LHC ring, and the y-axis points upward. Polar coordinates (r, ϕ) are used in the transverse (x,y)-plane, ϕ being the azimuthal angle around the beam pipe. The rapidity is defined as $y = 0.5 \times \ln[(E + p_z)/(E - p_z)]$, where E denotes the energy and p_z is the component of the momentum along the beam direction. The pseudorapidity is defined in terms of the polar angle θ as $\eta = -\ln\tan(\theta/2)$.

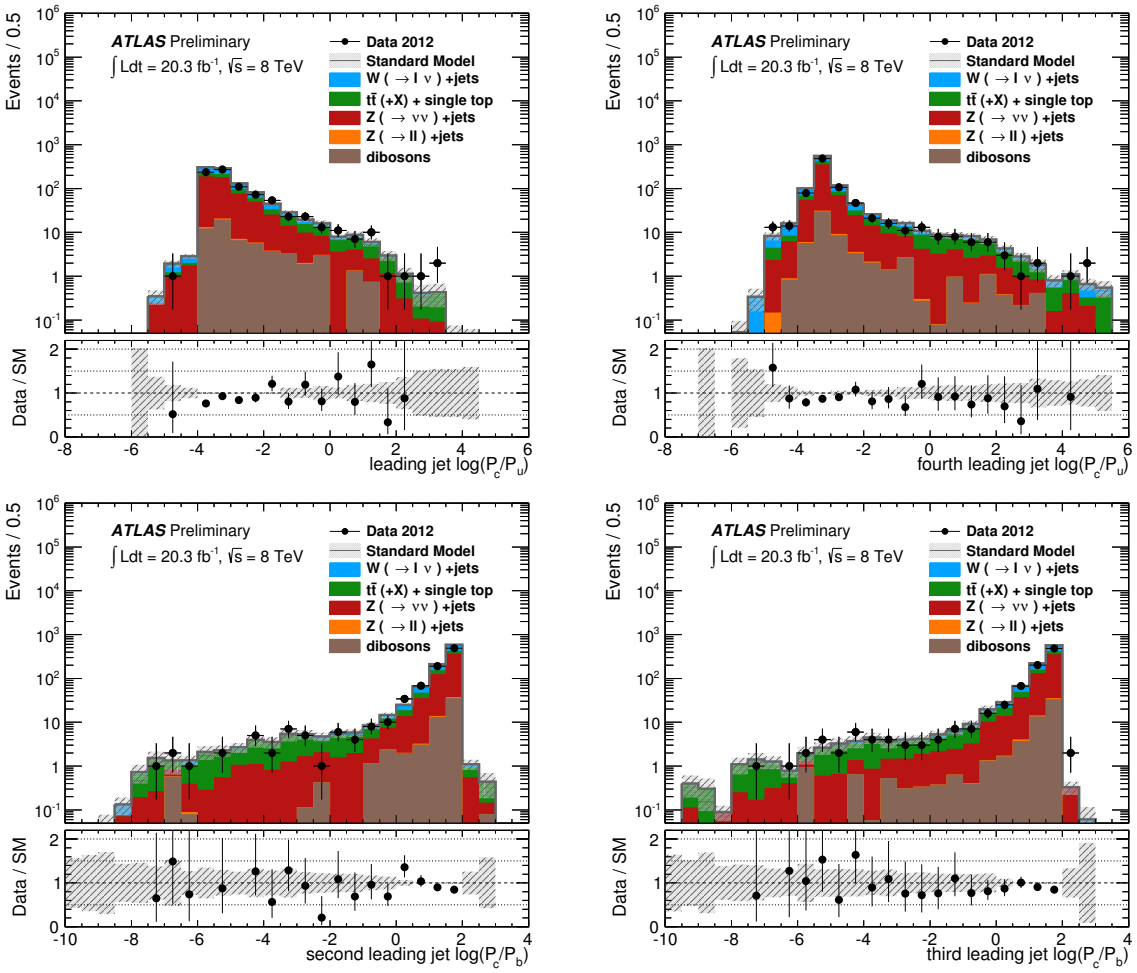

Figure 2: (Top) Distribution of the discriminator against light-jets, $\log(P_c/P_u)$, for the leading (left) and fourth leading jet (right). (Bottom) Distribution of the discriminator against b-jets, $\log(P_c/P_b)$, for the second (left) and third leading jet (right). The discriminators shown for the different jets follow the tagging criteria discussed in Section 4. The data are compared to MC simulations for the different SM processes and include the signal selection C1 defined in Section 4 without applying the tagging requirements. The error bands in the ratios include the statistical and experimental uncertainties in the predictions.

4 Event selection

The data sample used in this note was collected with the ATLAS detector and corresponds to a total integrated luminosity of 20.3 fb^{-1}. The uncertainty on the integrated luminosity is ±2.8%. It is estimated, following the same methodology as that detailed in Ref. [59], from a preliminary calibration of the luminosity scale derived from beam-separation scans performed in November 2012. The data were selected online using a trigger logic that selects events with $E_{\mathrm{T}}^{\mathrm{miss}}$ above 80 GeV, as computed at the final stage of the three-level trigger system of ATLAS [60]. With respect to the analysis requirements, the trigger selection is fully efficient, as determined using a data sample with muons in the final state. The following preselection criteria are applied.

- Events are required to have a reconstructed primary vertex [61] consistent with the beamspot envelope and having at least five tracks; when more than one such vertex is found, the vertex with the largest summed $|p_{\mathrm{T}}|^2$ of the associated tracks is chosen. This rejects beam-related backgrounds and cosmic rays.
- Events are required to have $E_{\mathrm{T}}^{\mathrm{miss}} > 150$ GeV and at least one jet with $p_{\mathrm{T}} > 120$ GeV and $|\eta| < 2.8$ in the final state.
- Events are rejected if they contain any jet with $p_{\mathrm{T}} > 20$ GeV and $|\eta| < 4.5$ that presents anomalous charged fraction, electromagnetic fraction in the calorimeter, or sampling fraction inconsistent with the requirement that they originate from a proton-proton collision. In the case of the leading jet in the event, the requirements are tightened to reject potentially remaining contributions from beam-related backgrounds and cosmic rays. Additional requirements are applied to suppress coherent noise and electronic noise bursts in the calorimeter producing anomalous energy deposits [62].
- Events with isolated electrons (muons) with $p_{\mathrm{T}} > 20$ GeV ($p_{\mathrm{T}} > 10$ GeV) are vetoed.

4.1 Monojet-like selection

The monojet-like analysis targets the region in which stop and lightest neutralino are nearly degenerate in mass so that c-jets are too soft to be tagged. Stop pair production events are then characterized by a small number of jets and can be identified via the presence of an energetic jet from initial state radiation. A maximum of three jets with $p_{\mathrm{T}} > 30$ GeV and $|\eta| < 2.8$ in the event is allowed. An additional requirement on the azimuthal separation of $\Delta\phi(\mathrm{jet}, \mathbf{p}_{\mathrm{T}}^{\mathrm{miss}}) > 0.4$ between the missing transverse momentum direction and that of each of the selected jets is set. This requirement reduces the multijet background contribution where the large $E_{\mathrm{T}}^{\mathrm{miss}}$ originates from mainly jet mismeasurement. A signal region (denoted M1) is defined with leading jet $p_{\mathrm{T}} > 280$ GeV and $E_{\mathrm{T}}^{\mathrm{miss}} > 220$ GeV, as the result of an optimization performed as a function of the $\tilde{t}$ and $\tilde{\chi}_1^0$ masses.

4.2 Charm-tagged selection

While the monojet-like selection has a relatively small signal to background ratio, the charm-tagged selection is designed to enhance the signal purity in the moderate Δm region. The kinematics of the charm jets from the stop decays depend mainly on Δm. As Δm decreases, the p_{T}'s of the charm jets become softer and it is more likely that more than one jet from initial state radiation has a higher transverse momentum than the charm jets. An optimization of the charm-tagged selection criteria is performed across the $\tilde{t}$ and $\tilde{\chi}_1^0$ mass plane to maximize the sensitivity to a SUSY signal.

A signal region (denoted C1) is defined by requiring $E_{\mathrm{T}}^{\mathrm{miss}} > 410$ GeV and a leading jet with $p_{\mathrm{T}} > 270$ GeV and $|\eta| < 2.8$. Three additional jets are required to have $p_{\mathrm{T}} > 30$ GeV and $|\eta| < 2.5$. As in the

monojet-like case, the azimuthal separation $\Delta\phi(\text{jet}, \mathbf{p}_{\text{T}}^{\text{miss}}) > 0.4$ between the $E_{\text{T}}^{\text{miss}}$ direction and that of each of the selected jets is required. Different tagging approaches are applied to the different jets. The leading jet tends to be an ISR jet, both for signal and background. Therefore, no tagging requirement is applied. The second and third leading-jets are required to have a *loose* charm-tag and the fourth leading jet is required to pass the *medium* charm-tagging requirement. The *loose* tags represent a b-jet veto which mainly serves to reject $t\bar{t}$ background, and the *medium* tag represents both a b-jet and a light-jet veto. It is applied to the fourth leading jet which is likely to be a charm-jet originating from a stop decay. While the ISR jet is selected in the region $|\eta| < 2.8$, the tagged jet requirement is tightened to $|\eta| < 2.5$ to be within the acceptance of the inner tracking detector.

Table 1 summarizes the different event selection criteria applied in the signal regions.

Selection criteria		
Preselection		
Primary vertex $E_{\text{T}}^{\text{miss}} > 120$ GeV Jet quality requirements At least one jet with $p_{\text{T}} > 120$ GeV and $\|\eta\| < 2.8$ Lepton vetoes: no isolated electrons (muons) with $p_{\text{T}} > 20$ GeV ($p_{\text{T}} > 10$ GeV)		
Monojet-like selection M1		Charm-tagged selection C1
At most three jets with $p_{\text{T}} > 30$ GeV and $\|\eta\| < 2.8$ $\Delta\phi(\text{jet}, \mathbf{p}_{\text{T}}^{\text{miss}}) > 0.4$		At least three jets with $p_{\text{T}} > 30$ GeVand $\|\eta\| < 2.5$ (in addition to the leading jet) b-veto for second and third jet *medium* c-tag for fourth jet $\Delta\phi(\text{jet}, \mathbf{p}_{\text{T}}^{\text{miss}}) > 0.4$
minimum leading jet p_{T} (GeV)	280	270
minimum $E_{\text{T}}^{\text{miss}}$ (GeV)	220	410

Table 1: Event selection criteria applied for the monojet-like and charm-tagged analyses.

5 Background estimation

The expected SM background is dominated by $Z(\to \nu\bar{\nu})$+jets, $t\bar{t}$ and $W(\to \ell\nu)$+jets ($\ell = e, \mu, \tau$) production, and include contributions from $Z/\gamma^*(\to \ell^+\ell^-)$+jets, multijet and diboson (WW, WZ, ZZ) processes. The W/Z plus jets backgrounds are estimated using MC event samples normalized using data in control regions. The top background contribution to the monojet-like analysis is very small and determined using MC simulated samples. In the case of the charm-tagged analysis the top background is sizable, as enhanced by the c-tagged requirements, and is estimated using MC simulated samples normalized in a top-enriched control region. The remaining SM backgrounds from dibosons are determined using Monte Carlo simulated samples, while the multijet background contribution is extracted from data. The normalization factors for the different background contributions are extracted simultaneously using a global fit to all control regions and including systematic uncertainties, to properly take into account correlations. Finally, the potential contributions from beam-related background and cosmic rays are estimated using data and found to be negligible.

5.1 Electroweak background

In the monojet-like analysis, control samples in data, orthogonal to the signal region, with identified electrons or muons in the final state and with the same requirements on the jet p_{T}, subleading jet ve-

toes, and $E_{\mathrm{T}}^{\mathrm{miss}}$, are used to determine the W/Z+jets electroweak background contributions from data. This reduces significantly the relatively large theoretical and experimental systematic uncertainties associated to purely MC-based predictions. A $W(\rightarrow \mu\nu)$+jets control sample is defined using events with a muon with $p_{\mathrm{T}} > 10$ GeV and transverse mass [2] in the range 30 GeV $< m_{\mathrm{T}} <$ 100 GeV. Similarly, a Z/γ^{*} $(\rightarrow \mu^{+}\mu^{-})$+jets control sample is selected requiring the presence of two muons with invariant mass in the range 66 GeV $< m_{\mu\mu} <$ 116 GeV. Finally, a $W(\rightarrow e\nu)$+jets dominated control sample is defined using events with an electron candidate with $p_{\mathrm{T}} > 20$ GeV. For the latter, the $E_{\mathrm{T}}^{\mathrm{miss}}$ calculation includes the contribution of the energy cluster from the identified electron in the calorimeter, that is treated as a jet, since $W(\rightarrow e\nu)$+jets processes contribute to the background in the signal region when the electron is not identified. In the $W(\rightarrow \mu\nu)$+jets and Z/γ^{*} $(\rightarrow \mu^{+}\mu^{-})$+jets control regions the $E_{\mathrm{T}}^{\mathrm{miss}}$ does not include muon contributions as they are considered invisible.

The definition of the control regions in the charm-tagged analysis follows closely that of the monojet-like approach. A tighter cut 81 GeV $< m_{\mu\mu} <$ 101 GeV is used to define the Z/γ^{*} $(\rightarrow \mu^{+}\mu^{-})$+jets control sample, as required to further reject $t\bar{t}$ contamination. In the charm-tagged analysis, the c-tagging is one of the major uncertainties and the same tagging criteria as used in the signal selection are applied to the $W(\rightarrow \mu\nu)$+jets, $W(\rightarrow e\nu)$+jets and Z/γ^{*} $(\rightarrow \mu^{+}\mu^{-})$+jets control regions. Since this increases significantly the statistical uncertainty in these control regions, the kinematic selections on the leading jet p_{T} and $E_{\mathrm{T}}^{\mathrm{miss}}$ are both reduced to 150 GeV for which the trigger selection still remains fully efficient. This implies the need for a MC-based extrapolation of the normalization factors, as determined using data at relatively low leading jet p_{T} and $E_{\mathrm{T}}^{\mathrm{miss}}$, to the signal region. The W/Z+jets MC samples in the charm-tagged analysis are reweighted to ensure that they properly describe the measured boson p_{T} distribution in the data, following the same procedure as described in Ref. [63], and leading to a very good description of the shape of the measured jet p_{T} and $E_{\mathrm{T}}^{\mathrm{miss}}$ distributions.

Monte Carlo-based transfer factors, determined by the `Sherpa` simulation, are defined for each of the signal selections to estimate the different electroweak background levels in the signal regions. As an example, in the case of the dominant $\mathrm{Z}(\rightarrow \nu\bar{\nu})$+jets background process, its contribution to a given signal region $N(\mathrm{Z}(\rightarrow \nu\bar{\nu}) + \mathrm{jets})_{signal}$ would be determined using the $W(\rightarrow \mu\nu)$+jets control sample in data according to

$$N(\mathrm{Z}(\rightarrow \nu\bar{\nu}) + \mathrm{jets})_{signal} = (N^{data}_{W\rightarrow\mu\nu,control} - N^{non-W}_{W\rightarrow\mu\nu,control}) \times \frac{N^{MC}(\mathrm{Z}(\rightarrow \nu\bar{\nu}) + \mathrm{jets})_{signal}}{N^{MC}_{W\rightarrow\mu\nu,control}}, \quad (1)$$

where $N^{MC}(\mathrm{Z}(\rightarrow \nu\bar{\nu}) + \mathrm{jets})_{signal}$ denotes the background predicted by the MC simulation in the signal region, and $N^{data}_{W\rightarrow\mu\nu,control}$, $N^{MC}_{W\rightarrow\mu\nu,control}$, and $N^{non-W}_{W\rightarrow\mu\nu,control}$ denote, in the control region, the number of $W(\rightarrow \mu\nu)$+jets candidates in data and MC simulation, and the non-$W(\rightarrow \mu\nu)$ background contribution, respectively. The latter refers mainly to top-quark and diboson processes, but also includes contributions from the rest of W/Z+jets processes. Therefore, the transfer factors for each process are defined as the ratio of simulated events for the process in the signal region over the total number of simulated events in the control region.

In the monojet-like analysis, the $W(\rightarrow \mu\nu)$+jets control sample is employed to define transfer factors for $W(\rightarrow \mu\nu)$+jets and Z $(\rightarrow \nu\bar{\nu})$+jets processes, and the $W(\rightarrow e\nu)$+jets control sample is used to constrain $W(\rightarrow e\nu)$+jets, $W(\rightarrow \tau\nu)$+jets, $Z/\gamma^{*}(\rightarrow \tau^{+}\tau^{-})$+jets, and Z/γ^{*} $(\rightarrow e^{+}e^{-})$+jets contributions. The Z/γ^{*} $(\rightarrow \mu^{+}\mu^{-})$+jets control sample is used to constrain the Z/γ^{*} $(\rightarrow \mu^{+}\mu^{-})$+jets background contribution and as an alternate estimate of the $Z(\rightarrow \nu\bar{\nu})$+jets and the rest of $Z/\gamma^{*}(\rightarrow \ell^{+}\ell^{-})$+jets background contributions (see Section 6). The charm-tagged analysis follows a similar approach to determine the normalization factors for each of the W/Z+jets background contributions. However, in this case the nominal

[2] The transverse mass m_{T} is defined by the lepton (ℓ) and neutrino (ν) p_{T} and direction as $m_T = \sqrt{2p^{\ell}_{\mathrm{T}}p^{\nu}_{\mathrm{T}}(1-\cos(\phi^{\ell}-\phi^{\nu}))}$, where the (x, y) components of the neutrino momentum are taken to be the same as the corresponding $E_{\mathrm{T}}^{\mathrm{miss}}$ components.

$Z(\rightarrow \nu\bar{\nu})$+jets normalization is extracted from the Z/γ^* $(\rightarrow \mu^+\,\mu^-)$+jets control sample, motivated by the fact that both processes involve identical heavy flavor production mechanisms.

Figures 3-5 show, for the different control samples, a number of selected distributions in data and MC simulations for the M1 selection. Similarly, the distribution of the leading jet p_{T} and $E_{\mathrm{T}}^{\mathrm{miss}}$ in the three control regions for the C1 selection are shown in Fig. 6. The W/Z+jets predictions are obtained using `Sherpa` and include the data-driven normalization factors.

5.2 Top quark background

As already mentioned, the background contribution of top quark production processes to the monojet-like selection is small and is enterely determined from MC. In the case of the charmed-tagged analysis, the MC predictions are normalized to the data in a separate control region. For this $t\bar{t}$ control region, b-tagging is used to yield a high-purity control region with negligible signal contamination. In addition to lowering the leading jet p_{T} and $E_{\mathrm{T}}^{\mathrm{miss}}$ requirements both to 150 GeV, c-tagging is replaced by b-tagging by inverting the loose c-tagging criterion: the inverted b-veto is thereby converted into a b-identification requirement. For this control region, at least two b-tagged jets among the three leading jets need to be identified. The distributions of the leading jet p_{T} and $E_{\mathrm{T}}^{\mathrm{miss}}$ for this $t\bar{t}$ control region are shown in Fig. 7.

5.3 Multijets background

The multijet background events can enter the signal regions if one of the jets is mis-measured, producing fake $E_{\mathrm{T}}^{\mathrm{miss}}$, and from events containing true $E_{\mathrm{T}}^{\mathrm{miss}}$(neutrinos from heavy flavour decays). The background is determined mainly from data, with minimal dependence on the MC simulation. This technique, which is referred to as the *jet smearing* method, has been used in other SUSY searches [64]. It relies on the assumption that the $E_{\mathrm{T}}^{\mathrm{miss}}$ of multijet events is dominated by jet fluctuations (true or fake) and that those fluctuations can be measured in the data. The method proceeds as follows:

1. A sample of low-$E_{\mathrm{T}}^{\mathrm{miss}}$ seed events is selected from data.

2. A response function, R, which quantifies the fluctuation in measured jet p_{T}, is measured. This response function includes effects of jet mis-measurements and contribution from neutrinos in heavy flavour decays. An initial estimate of the response function is obtained from the MC simulation.

3. The response function is modified by smearing the seed events, until good agreement is observed between smeared data and data in control regions sensitive to this jet response.

4. Seed events are then smeared with the adjusted response function from (3).

Seed events are selected with single jet triggers and low $E_{\mathrm{T}}^{\mathrm{miss}}$ significance, $E_{\mathrm{T}}^{\mathrm{miss}}/\sqrt{\sum E_T}$, where $\sum E_T$ denotes the scalar sum of the transverse energy in the detector. Here $E_{\mathrm{T}}^{\mathrm{miss}}$ significance is preferred over $E_{\mathrm{T}}^{\mathrm{miss}}$ itself to avoid biasing the jet p_{T} distribution. Two response functions are used, one for jets with b-veto and another for b-tagged jets. At least 250 smeared events are produced from each seed event. These events are normalised to data in a multijet dominated control region, defined by small $\Delta\phi$(jet, $\mathbf{p}_{\mathrm{T}}^{\mathrm{miss}}$). The contribution from other backgrounds is subtracted using MC simulations. This sample is then used to estimate the multijets background in the different selections. For the monojet-like analysis, it constitutes less than 1% of the total background and it is negligible in the charm-tagged case.

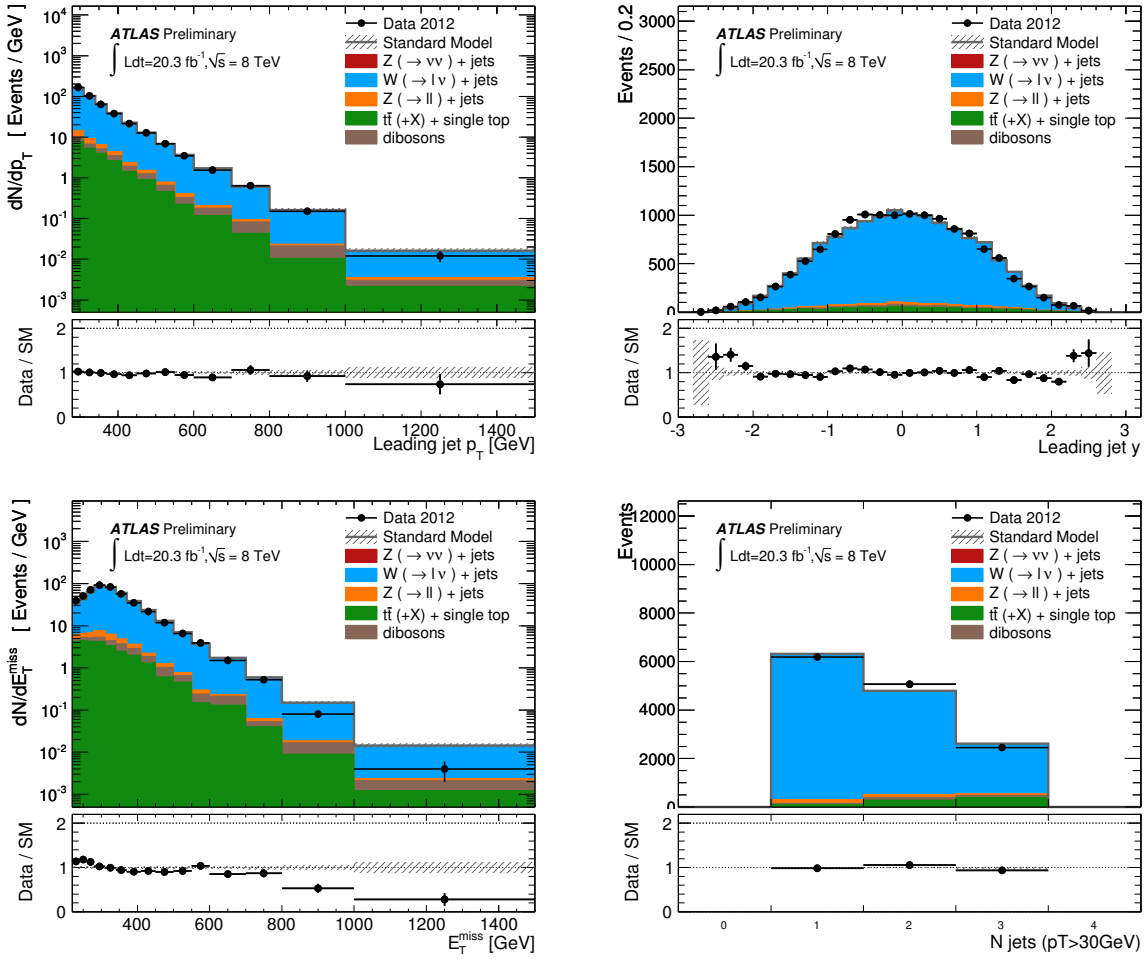

Figure 3: The leading jet p_{T} and y, $E_{\mathrm{T}}^{\mathrm{miss}}$, and jet multiplicity distributions in the $W(\rightarrow \mu\nu)$+jet control region, for the M1 selection, compared to the background predictions. The latter include the global normalization factors extracted from the fit (see Section 6). The error bands in the ratios include the statistical and experimental uncertainties on the background predictions.

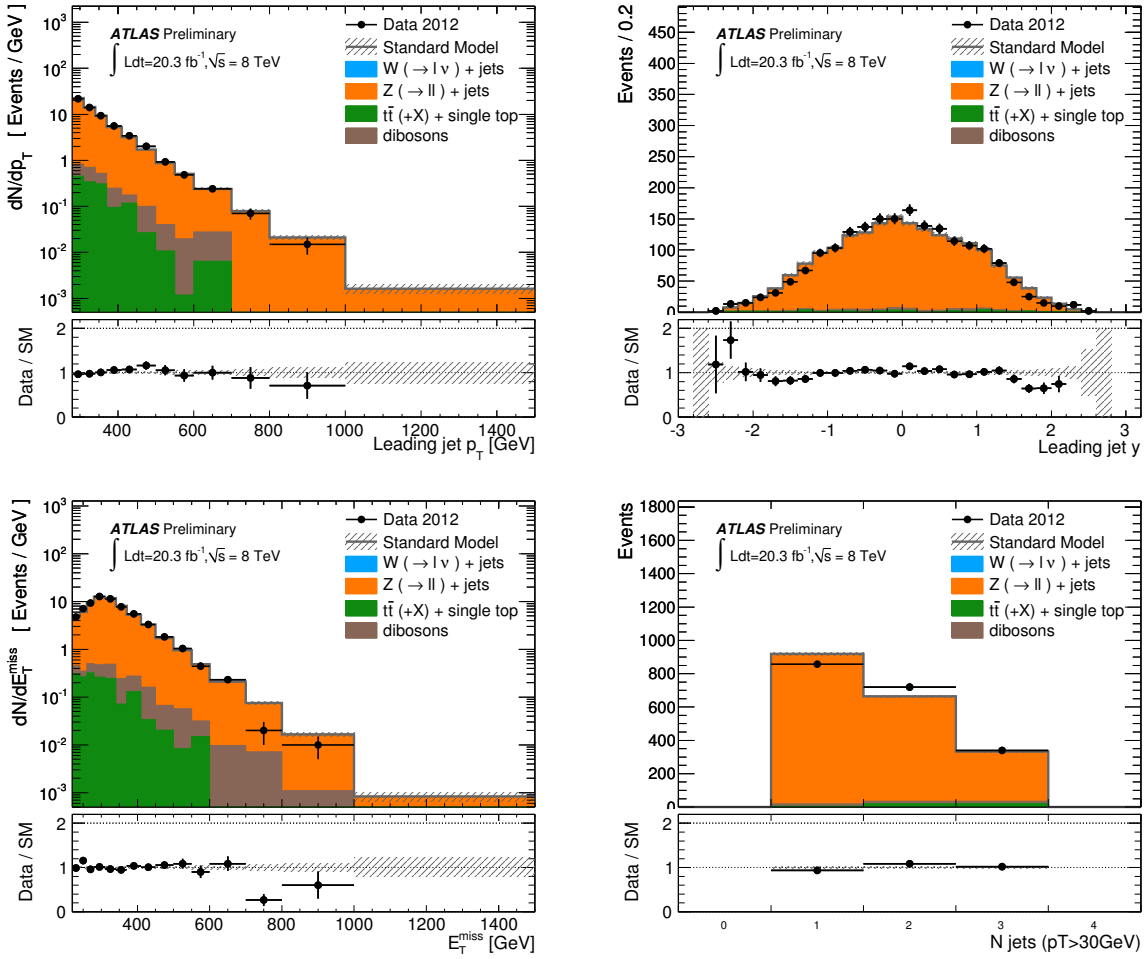

Figure 4: The measured leading jet p_{T} and y, $E_{\mathrm{T}}^{\mathrm{miss}}$, and jet multiplicity distributions in the Z/γ^{*} ($\rightarrow \mu^{+}\mu^{-}$)+jet control region, for the M1 selection, compared to the background predictions. The latter include the global normalization factors extracted from the fit (see Section 6). The error bands in the ratios include the statistical and experimental uncertainties on the background predictions.

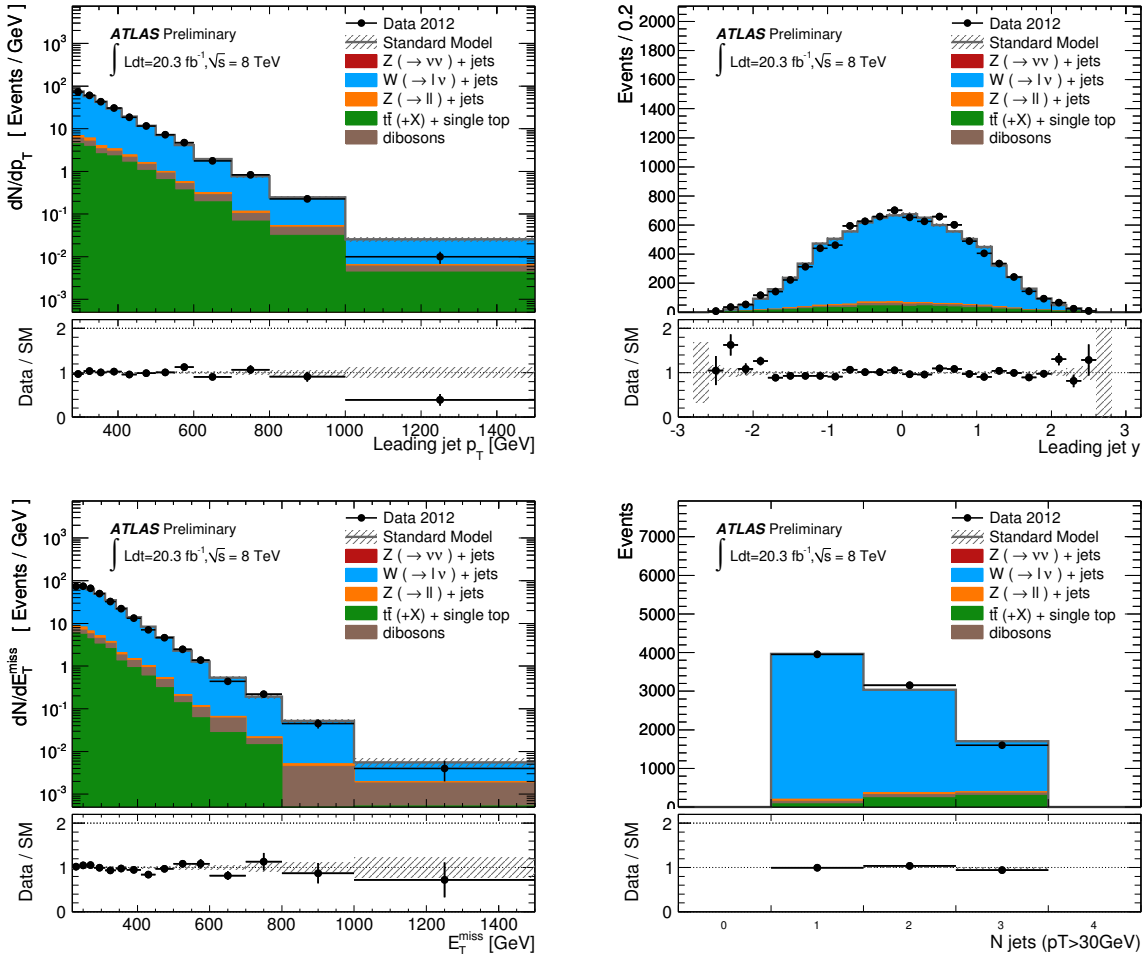

Figure 5: The measured leading jet p_{T} and y, $E_{\mathrm{T}}^{\mathrm{miss}}$, and jet multiplicity distributions in the $W(\rightarrow e\nu)$+jet control region, for the M1 selection, compared to the background predictions. The latter include the global normalization factors extracted from the fit (see Section 6). The error bands in the ratios include the statistical and experimental uncertainties on the background predictions.

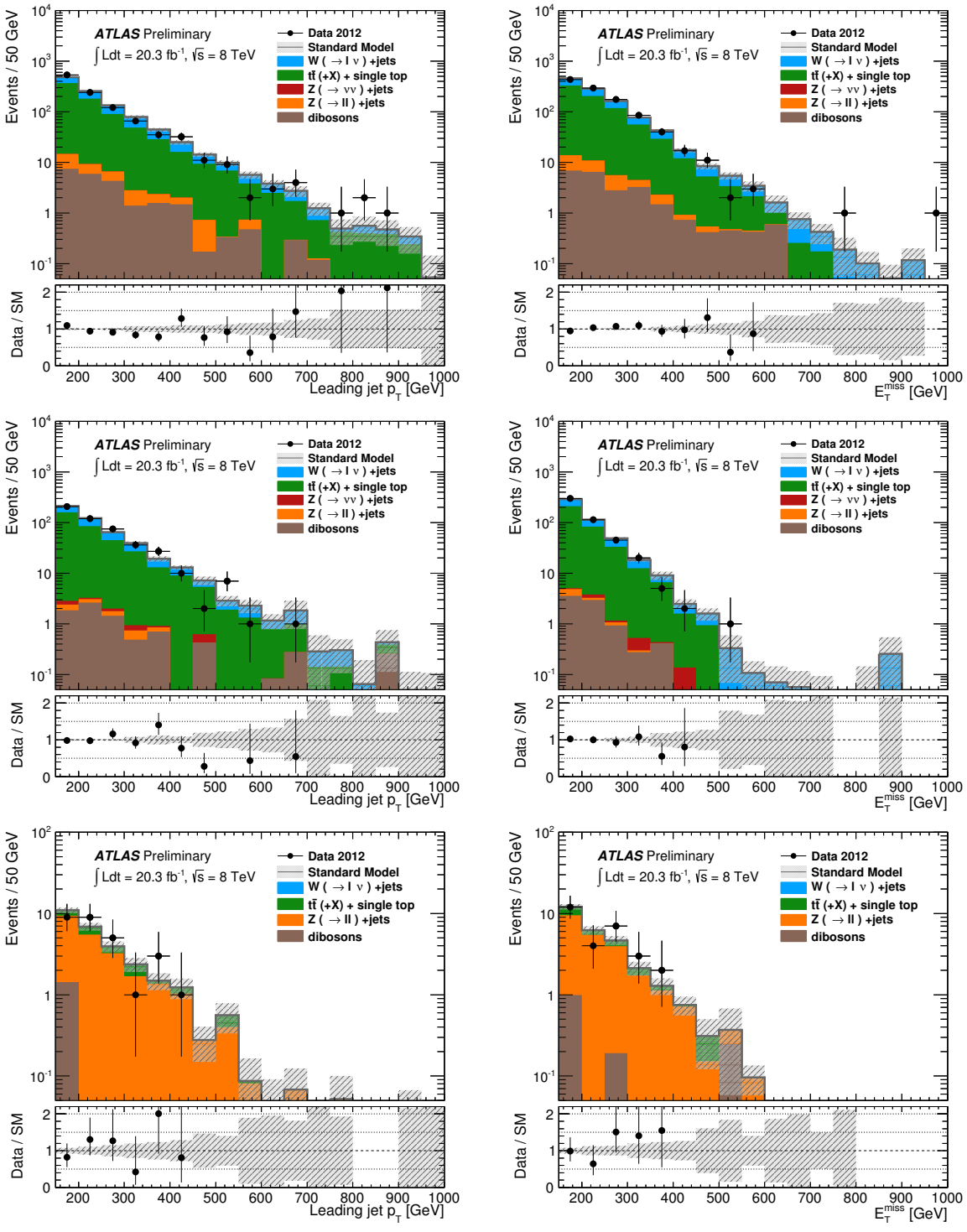

Figure 6: The leading jet p_{T} and $E_{\mathrm{T}}^{\mathrm{miss}}$ distributions for the c-tag $W(\rightarrow \mu\nu)$+jets (top) $W(\rightarrow e\nu)$+jets (middle) and Z/γ^{*} $(\rightarrow \mu^{+}\mu^{-})$+jets (bottom) control regions, compared to the background predictions. The predictions include the global normalization factors extracted from the fit (see Section 6). The error bands in the ratios include the statistical and experimental uncertainties on the background predictions.

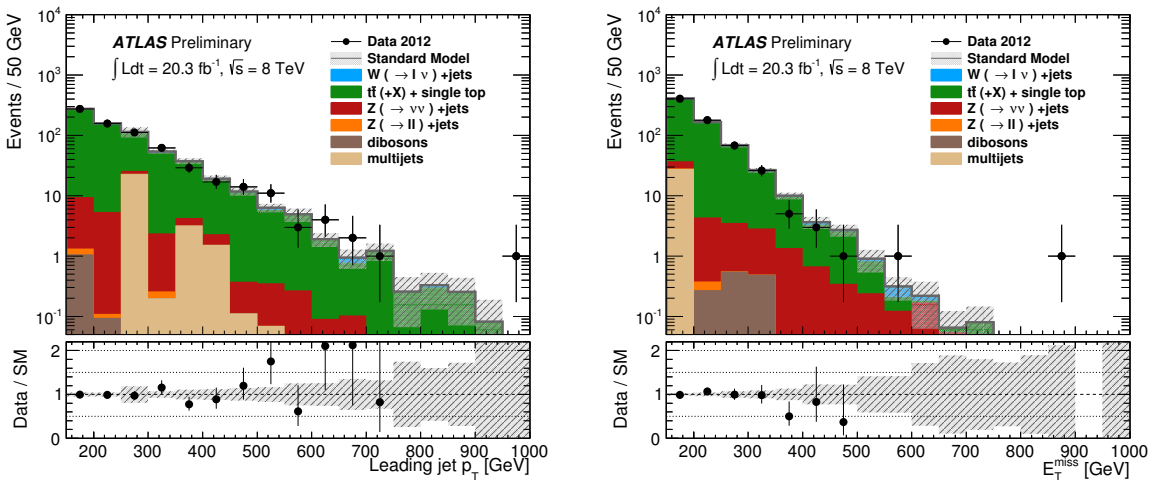

Figure 7: The leading jet p_{T} and $E_{\mathrm{T}}^{\mathrm{miss}}$ distributions for the $t\bar{t}$ control region in the c-tag analysis, compared to the background predictions. The predictions include the global normalization factors extracted from the fit (see Section 6). The error bands in the ratios include the statistical and experimental uncertainties on the background predictions.

6 Systematic uncertainties

A complete study of systematic uncertainties was carried out in the monojet-like and charm-tagged analyses. Since the normalization of the dominant backgrounds, $Z(\rightarrow \nu\bar{\nu})$+jets, W+jets production, (and $t\bar{t}$ in the case of the charm-tagged analysis) is obtained from control regions, the theoretical and modelling uncertainties that introduce a difference in acceptance between the control regions and the signal regions are the dominating sources of systematic uncertainty on the total background prediction. In the following, the impact of each source of systematic uncertainty on the SM background prediction in each analysis is discussed separately. To determine the final uncertainty on the total background, all systematic uncertainties are then treated as nuisance parameters with Gaussian shapes in a fit based on the profile likelihood method [65], that takes into account correlations among systematic variations. A simultaneous likelihood fit to the $W(\rightarrow \mu\nu)$+jets, $W(\rightarrow e\nu)$+jets, Z/γ^{*} $(\rightarrow \mu^{+}\mu^{-})$+jets and $t\bar{t}$ control regions (the latter in the case of the charm-tagged analysis) is performed separately for each analysis to normalize and constrain the corresponding background estimates in the signal regions. The results of the fits are collected in Tables 2 and 3 for the M1 and C1 selections, respectively.

6.1 Monojet-like analysis

Different sources of systematic uncertainty are considered in the determination of the background contributions. Uncertainties in the absolute jet and $E_{\mathrm{T}}^{\mathrm{miss}}$ energy scale and resolution [50] translate into an uncertainty on the total background of about 0.7%. Uncertainties on pile-up corrections to the jet p_{T} and $E_{\mathrm{T}}^{\mathrm{miss}}$ introduce an about 1.5% uncertainty on the background predictions. Uncertainties in the simulated lepton identification efficiencies translate into a 1.5% uncertainty in the total background. The dependence of the predicted W/Z+jets backgrounds on the parton shower and hadronization model used in the MC simulations is studied by comparing the predictions from `Sherpa` and `Alpgen`. Variations of the renormalization/factorization and parton-shower matching scales in the simulated samples are also explored. The differences in the $Z(\rightarrow \nu\bar{\nu})$+jets and $Z/\gamma^{*}(\rightarrow \ell^{+}\ell^{-})$+jets backgrounds, as predicted using the $W(\rightarrow \mu\nu)$ or Z/γ^{*} $(\rightarrow \mu^{+}\mu^{-})$ control regions, are included as an additional uncertainty. Altogether, this

translates into a 1.8% uncertainty on the total background. Uncertainties on the modelling of top-quark related processes, as determined by comparing Powheg and MC@NLO predictions, and a 10% uncertaintly on the top production cross section translate into a 0.5% uncertainty on the background prediction. A 50% uncertaintly on the diboson contribution is considered which constitutes a 0.4% uncertainty on the total background. Finally, a conservative 100% uncertainty on the multijet background estimation is adopted leading to a 1.1% uncertainty on the total background. Other sources of uncertainty related to the trigger efficiency and a 2.8% uncertainty on the total luminosity determination [59] cancel out in the data-driven method.

6.2 Charm-tagged analysis

The experimental uncertanties that affect the background yields are dominated by the uncertainties in jet energy scale and c-tagging. The jet energy scale uncertainty translates into a 15% uncertainty in the final background estimate. Uncertainties related to the *loose* and *medium* c-tag introduce a 8% and 4% uncertainty on the background yield, respectively. Uncertainties related to the jet energy resolution, modelling of multiple pp interactions, trigger and lepton reconstruction and identification (momentum and energy scales, resolutions and efficiencies) and total integrated luminosity give contributions below 2%. For the Z+jets and W+jets background, the theoretical and MC modelling uncertainties are estimated by comparing the event generators Sherpa and Alpgen; this difference translates into an uncertainty on the Z+jets and W+jets background yields of 11% and 9%, respectively. Uncertainties in the re-weighting of the simulated W and Z p_{T} distributions introduce an additional 2.5% uncertainty in the final background estimates. For the c-tagged analysis the Z+jets and W+jets background is enriched in heavy flavor jets produced in association with the vector boson and the same heavy flavor contributions are present in the signal region and the V+jets control regions. For $t\bar{t}$ processes the uncertainties are evaluated by comparing different event generators (Powheg and Alpgen), parton shower modelling (Pythia and Herwig), by varying ISR/FSR and QCD scale parameters and they translate into an uncertainty on the transfer factor of 10% to 35%, leading to a 2% to 8% uncertainty on the final background estimate. Electroweak single top and diboson production are associated with theoretical cross-section uncertainties as given in Section 2. For the single top acceptance, twice the uncertainty of the $t\bar{t}$ background is assumed. For dibosons the uncertainties are evaluated by comparing different event generators (Herwig and Alpgen) and by varying QCD scale parameters. This results in less than 5% uncertainties on the total background prediction in the signal region. Additional sub-dominant uncertainties are due to the limited statistics of the SM MC samples and of the data in the control regions. As already mentioned, the background from multijet processes is negliglible.

In the case of the charm-tagged analysis, for which the control regions are defined with lower thresholds on the leading jet p_{T} and $E_{\mathrm{T}}^{\mathrm{miss}}$ compared to those of the C1 signal region, the $W(\rightarrow \mu\nu)$+jets, $W(\rightarrow e\nu)$+jets, Z/γ^{*} $(\rightarrow \mu^{+}\,\mu^{-})$+jet and $t\bar{t}$ yields fitted in the control regions are validated in three dedicated validation regions (denoted as V1 – V3) that differ from the signal region C1 only in the requirements on $E_{\mathrm{T}}^{\mathrm{miss}}$ and the leading jet p_{T}. The validation regions are defined such that there is no event overlap with the signal region nor control regions. The results are collected in Table 4 showing a good understanding of the background yields.

Monojet-like control regions	$W(\rightarrow e\nu)$+jets	$W(\rightarrow \mu\nu)$+jets	Z/γ^* ($\rightarrow \mu^+\mu^-$)+jets
Observed events (20.3 fb^{-1})	8707	13703	1916
SM prediction (post-fit)	8710 ± 95	13700 ± 122	1920 ± 44
Fitted $W(\rightarrow e\nu)$	6230 ± 144	0.3 ± 0.2	–
Fitted $W(\rightarrow \mu\nu)$	40 ± 17	11420 ± 310	2.4 ± 1.4
Fitted $W(\rightarrow \tau\nu)$	1470 ± 54	950 ± 192	0.6 ± 0.4
Fitted $Z(\rightarrow \nu\bar{\nu})$	16 ± 16	3.4 ± 2.2	–
Fitted Z/γ^* ($\rightarrow e^+e^-$)	0.01 ± 0.04	–	–
Fitted Z/γ^* ($\rightarrow \mu^+\mu^-$)	2.4 ± 1.4	270 ± 14	1830 ± 51
Fitted $Z/\gamma^*(\rightarrow \tau^+\tau^-)$	114 ± 8	40 ± 27	2.7 ± 1.6
Expected top	620 ± 77	770 ± 94	34 ± 4
Expected dibosons	210 ± 107	250 ± 126	50 ± 23
Expected multijets	–	–	–
SM prediction (pre-fit)	9786	15688	2137
Fit input $W(\rightarrow e\nu)$	7084	0.3	–
Fit input $W(\rightarrow \mu\nu)$	46	13232	2.8
Fit input $W(\rightarrow \tau\nu)$	1675	1080	0.7
Fit input $Z(\rightarrow \nu\bar{\nu})$	18	3.9	–
Fit input Z/γ^* ($\rightarrow e^+e^-$)	0.01	–	–
Fit input Z/γ^* ($\rightarrow \mu^+\mu^-$)	2.7	306	2051
Fit input $Z/\gamma^*(\rightarrow \tau^+\tau^-)$	129	41	3.0
Fit input top	616	770	34
Fit input dibosons	214	253	46
Fit input multijets	–	–	–

Table 2: Data and background predictions in the control regions before and after the fit is performed for the M1 selection. The background predictions include both statistical and systematic uncertainties. Note that the individual uncertainties can be correlated, and do not necessarily add up quadratically to the total background uncertainty.

Charm-tagged control regions	$W(\rightarrow \mu\nu)$+jets	$W(\rightarrow e\nu)$+jets	$t\bar{t}$	Z/γ^* ($\rightarrow \mu^+\mu^-$)+jets
Observed events (20.3 fb^{-1})	1060	485	685	28
SM prediction (post-fit)	1060 ± 32	485 ± 22	685 ± 26	28 ± 5
Fitted $W(\rightarrow e\nu)$	–	120 ± 54	4.0 ± 2.2	–
Fitted $W(\rightarrow \mu\nu)$	270 ± 110	0.1 ± 0.1	5.0 ± 2.5	0.09 ± 0.07
Fitted $W(\rightarrow \tau\nu)$	27 ± 13	17 ± 7	15 ± 9	–
Fitted $Z(\rightarrow \nu\bar{\nu})$	0.03 ± 0.01	1.3 ± 0.4	21 ± 7	–
Fitted Z/γ^* ($\rightarrow e^+e^-$)	–	–	–	–
Fitted Z/γ^* ($\rightarrow \mu^+\mu^-$)	9.0 ± 2.5	–	–	22 ± 5
Fitted $Z/\gamma^*(\rightarrow \tau^+\tau^-)$	8.0 ± 3.4	1.8 ± 0.8	0.5 ± 0.3	–
Fitted $t\bar{t}$	660 ± 110	310 ± 52	560 ± 35	4.3 ± 0.8
Fitted $t\bar{t}$+V	6.1 ± 1.1	2.9 ± 0.5	5.0 ± 0.3	0.4 ± 0.1
Fitted single top	56 ± 9	28 ± 5	48 ± 3	–
Expected dibosons	24 ± 4	8.2 ± 1.4	1.4 ± 0.4	1.4 ± 0.2
Expected multijets	–	–	28 ± 15	–
SM prediction (pre-fit)	1023	487	658	24
Fit input $W(\rightarrow e\nu)$	–	132	4.4	–
Fit input $W(\rightarrow \mu\nu)$	262	0.1	4.7	0.09
Fit input $W(\rightarrow \tau\nu)$	30	19	17	–
Fit input $Z(\rightarrow \nu\bar{\nu})$	0.02	1.0	17	–
Fit input Z/γ^* ($\rightarrow e^+e^-$)	–	–	–	–
Fit input Z/γ^* ($\rightarrow \mu^+\mu^-$)	7.3	–	–	18
Fit input $Z/\gamma^*(\rightarrow \tau^+\tau^-)$	8.5	2.0	0.5	–
Fit input $t\bar{t}$	631	295	534	4.1
Fit input $t\bar{t}$+V	5.9	2.8	4.8	0.4
Fit input single top	54	27	46	–
Fit input dibosons	24	8.2	1.4	1.4
Fit input multijets	–	–	28	–

Table 3: Data and background predictions in the control regions before and after the fit is performed for the C1 selection. The background predictions include both statistical and systematic uncertainties. Note that the individual uncertainties can be correlated, and do not necessarily add up quadratically to the total background uncertainty.

Charm-tagged validation regions	V1	V2	V3
$E_{\mathrm{T}}^{\mathrm{miss}}$ (GeV)	$\in [200, 290]$	$\in [200, 410]$	> 200
leading jet p_{T} (GeV)	$\in [200, 290]$	> 150	$\in [150, 270]$
Observed events	217	723	486
SM prediction (post-fit in control regions)	204 ± 28	674 ± 93	463 ± 67
$W(\rightarrow e\nu)$	6.4 ± 3.2	20 ± 10	13 ± 7
$W(\rightarrow \mu\nu)$	6.5 ± 2.9	24 ± 11	16 ± 7
$W(\rightarrow \tau\nu)$	47 ± 23	141 ± 69	93 ± 45
$Z(\rightarrow \nu\bar{\nu})$	38 ± 19	133 ± 61	88 ± 43
Z/γ^* $(\rightarrow\ e^+\, e^-)$	–	–	–
Z/γ^* $(\rightarrow\ \mu^+\, \mu^-)$	–	0.2 ± 0.1	0.10 ± 0.04
$Z/\gamma^*(\rightarrow \tau^+\tau^-)$	1.1 ± 0.5	3.0 ± 1.5	2.1 ± 1.0
$t\bar{t}$	91 ± 18	299 ± 69	214 ± 52
$t\bar{t} + V$	1.1 ± 0.2	4.5 ± 0.8	3.3 ± 0.6
single top	6.9 ± 1.2	24 ± 4	16 ± 3
dibosons	5.9 ± 0.8	23 ± 3	17 ± 2
multijets	–	2.9 ± 2.2	–
SM prediction (pre-fit in control regions)	205	672	460
$W(\rightarrow e\nu)$	7.8	24	16
$W \rightarrow \mu\nu$	6.7	25	16
$W(\rightarrow \tau\nu)$	57	171	112
$Z(\rightarrow \nu\bar{\nu})$	34	118	78
Z/γ^* $(\rightarrow\ e^+\, e^-)$	–	–	–
Z/γ^* $(\rightarrow\ \mu^+\, \mu^-)$	–	0.1	0.07
$Z/\gamma^*(\rightarrow \tau^+\tau^-)$	1.3	3.6	2.5
$t\bar{t}$	85	278	199
$t\bar{t} + V$	1.0	4.2	3.1
single top	6.5	22	15
dibosons	6.0	23	18
multijets	–	2.9	–

Table 4: Data and background predictions in the charm-tagged V1 – V3 validation regions. The background predictions include both statistical and systematic uncertainties. Note that the individual uncertainties can be correlated, and do not necessarily add up quadratically to the total background uncertainty.

Signal Region	M1	C1
Observed events (20.3 fb^{-1})	30793	25
SM prediction	29800 ± 900	29 ± 7
$W(\rightarrow e\nu)$	2700 ± 420	0.5 ± 0.3
$W(\rightarrow \mu\nu)$	2900 ± 330	0.8 ± 0.4
$W(\rightarrow \tau\nu)$	6600 ± 300	7 ± 4
$Z(\rightarrow \nu\bar{\nu})$	15600 ± 900	10 ± 5
Z/γ^* $(\rightarrow\ e^+\,e^-)$	–	–
Z/γ^* $(\rightarrow\ \mu^+\,\mu^-)$	50 ± 28	0.01 ± 0.01
$Z/\gamma^*(\rightarrow \tau^+\tau^-)$	80 ± 24	0.09 ± 0.04
top	700 ± 86	7 ± 3
dibosons	900 ± 420	2 ± 2
multijets	340 ± 340	–

Table 5: Data and background predictions in the signal region for the M1 and C1 selections. For the SM predictions both statistical and systematic uncertainties are included. Note that the individual uncertainties can be correlated, and do not necessarily add up quadratically to the total background uncertainty.

7 Results

The data and the expected background predictions for the monojet-like and charm-tagged analyses are summarized in Table 5. The SM predictions for the M1 and C1 selections are determined with a total uncertainty of 3% and 24%, respectively. Good agreement is observed between the data and the SM predictions in each case. Figure 8 shows the measured leading jet p_{T} and $E_{\mathrm{T}}^{\mathrm{miss}}$ distributions for the monojet-like and charm-tagged selections compared to the background predictions. For illustration purposes, the impact of two different SUSY scenarios with stop mass 200 GeV and neutralino masses 125 GeV and 195 GeV, respectively, are included.

The agreement between the data and the SM predictions for the total number of events in the different analyses is translated into 95% confidence level (CL) upper limits on the visible cross section, defined as the production cross section times acceptance times efficiency ($\sigma \times A \times \epsilon$), using the CL_s modified frequentist approach [66] and considering the systematic uncertainties on the SM backgrounds and a 2.8% uncertainty on the quoted integrated luminosity. Values of $\sigma \times A \times \epsilon$ above 136 fb and 0.7 fb are excluded at 95% CL for M1 and C1, selections, respectively (see Table 6).

The results are then translated into limits on the SUSY stop pair production with $\tilde{t} \rightarrow c\,\tilde{\chi}_1^0$ (BR=100%) as a function of the stop mass for different neutralino masses. Different sources of systematic uncertainty on the predicted SUSY signals are considered. Experimental uncertainties related to the jet and $E_{\mathrm{T}}^{\mathrm{miss}}$ scales and resolutions introduce uncertainties in the signal yields of 3% and 13% for the monojet-like and charm-tagged analyses, respectively. In the charm-tagged analysis, uncertainties on the simulated c-tagging efficiency for *loose* (*medium*) tag introduce a 7% (10%) uncertainty in the signal yields. In addition, a 2.8% uncertainty on the integrated luminosity is included. Uncertainties on the signal $A \times \epsilon$ related to the generation of the SUSY samples are determined using additional samples with modified parameters. This includes uncertainties on the modelling of the initial- and final-state gluon radiation (ISR and FSR), the choice of renormalization/factorization scales, and the parton-shower matching scale settings. Altogether this translates into an uncertainty on the signal yields that varies between 2% and 10% in the monojet-like analysis, and betweeen 8% and 29% in the charm-tagged selection, depending on the stop and neutralino masses. Finally, uncertainties on the predicted SUSY signal cross sections include PDF uncertainties, variations on the $\alpha_s(M_Z)$ value employed, as well as variations of the renor-

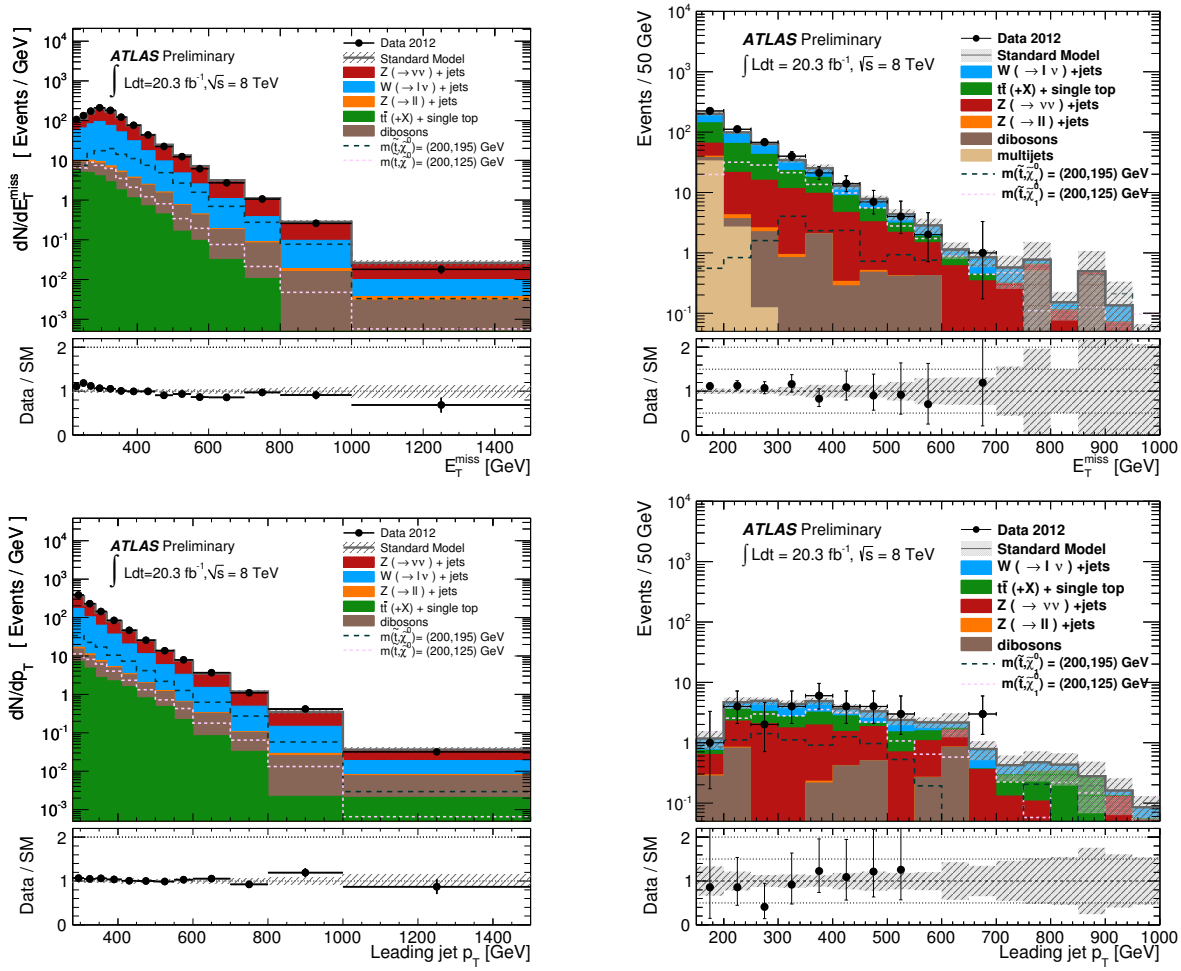

Figure 8: Measured $E_{\mathrm{T}}^{\mathrm{miss}}$ and leading jet p_{T} distributions for the M1 (left) and C1 (right) selections compared to the SM predictions. For the latter, the full signal selection is applied but the leading jet p_{T} is shown down to a value of 150 GeV and the missing transverse energy is also shown down to a value of 150 GeV. For illustration purposes, the impact of two different SUSY scenarios are included. The error bands in the ratios include both the statistical and systematic uncertainties on the background predictions.

Signal channel	$\langle\epsilon\sigma\rangle^{95}_{\rm obs}$[fb]	$S^{95}_{\rm obs}$	$S^{95}_{\rm exp}$	CL_B
M1	136	2770	2060^{+780}_{-570}	0.82
C1	0.7	13	14^{+5}_{-4}	0.45

Table 6: Left to right: 95% CL upper limits on the visible cross section ($\langle\epsilon\sigma\rangle^{95}_{\rm obs}$) and on the number of signal events ($S^{95}_{\rm obs}$). The third column ($S^{95}_{\rm exp}$) shows the 95% CL upper limit on the number of signal events, given the expected number (and $\pm1\sigma$ excursions on the expectation) of background events. The last column indicates the CL_B value, i.e. the confidence level observed for the background-only hypothesis.

malization and factorization scales by factors of two and one-half. Altogether, this results in a total theoretical uncertainty that varies between 14% and 16% for stop masses in the range between 100 GeV and 400 GeV.

Expected and observed 95% CL exclusion limits are set on the stop-neutralino mass plane for the process $\tilde{t} \rightarrow c + \chi^0_1$. The CL_s approach is used, including statistical and systematic uncertainties. For the latter, the uncertainties on the signal acceptance times efficiency, the background predictions, and the luminosity are considered, and correlations between systematic uncertainties on signal and background predictions are taken into account. In addition, observed limits are computed using $\pm1\sigma$ variations on the theory predictions for the SUSY cross sections. For each SUSY point considered, observed and expected limits are computed separately for the monojet-like and charm-tagged analyses, and the one with the best expected limit is adopted as the nominal result. As anticipated, the monojet-like selection drives the exclusion limits at very low Δm. The charm-tagged results determine the exclusion limits in the rest of the plane. Figure 9 presents the combined results. Masses for the stop up to 200 GeV are excluded at 95% CL for arbitrary neutralino masses, within the kinematic boundaries. For neutralino masses of about 200 GeV, stop masses below 230 GeV are excluded at 95% CL. These results extend significantly previous exclusion limits on the stop and neutralino masses from the Tevatron experiments in this channel.

8 Summary and conclusions

In summary, this note reports preliminary results on the search for stop pair production in the decay channel $\tilde{t} \rightarrow c + \chi^0_1$ using 20.3 fb^{-1} of proton-proton collision data at $\sqrt{s} = 8$ TeV recorded with the ATLAS experiment at the LHC. Different analyses are carried out that optimize the sensitivity across the stop-neutralino mass plane. Good agreement is observed between the data and the SM predictions. The results are translated into new 95% CL exclusion limits on the stop and neutralino masses. A top squark mass of 200 GeV is excluded at 95% confidence level for $m_{\tilde{t}}$–$m_{\tilde{\chi}^0_1} < 85$ GeV. Top squark masses up to 230 GeV are excluded for a neutralino mass of 200 GeV. This extends significantly previous Tevatron results.

References

[1] H. Miyazawa, *Baryon Number Changing Currents*, Prog. Theor. Phys. **36 (6)** (1966) 1266–1276.

[2] P. Ramond, *Dual Theory for Free Fermions*, Phys. Rev. **D3** (1971) 2415–2418.

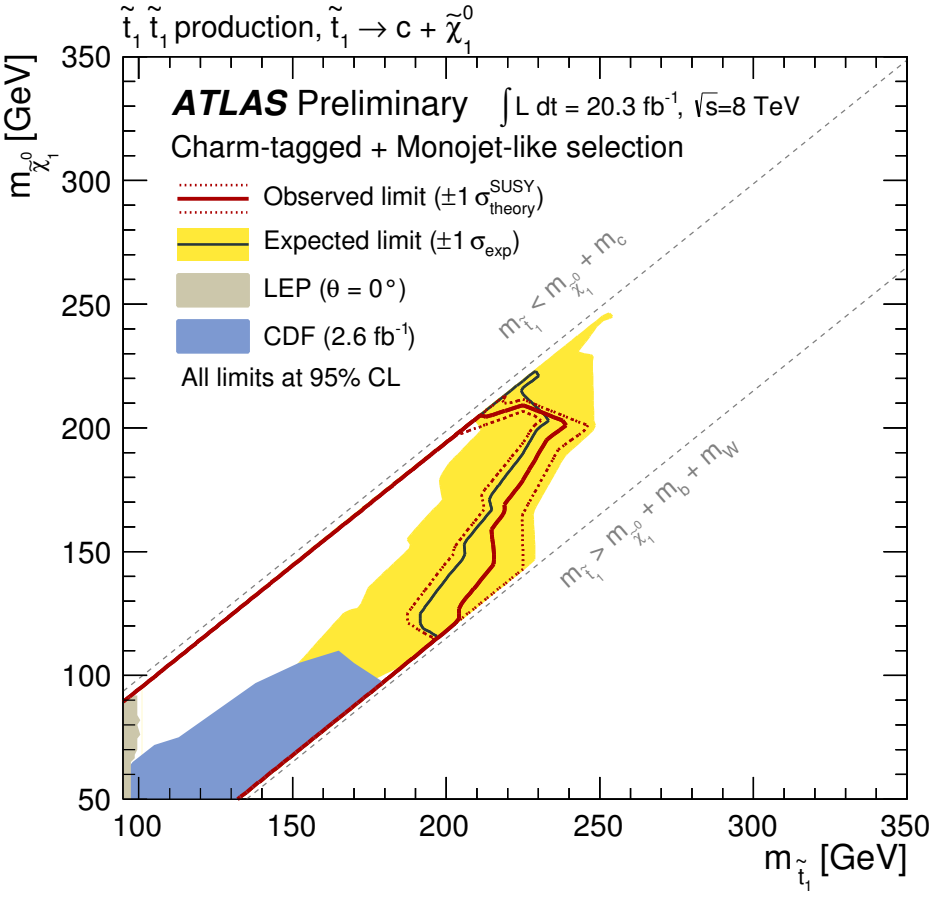

Figure 9: Exclusion plane at 95% CL. as a function of stop and neutralino masses. The observed (red line) and expected (black line) upper limits from this analysis are compared to previous results from Tevatron experiments [18, 19], and from LEP [67] experiments at CERN with squark mixing angle θ^o. The dotted lines around the observed limit indicate the range of observed limits corresponding to $\pm1\sigma$ variations on the NLO SUSY cross section predictions. The shaded area around the expected limit indicates the expected $\pm1\sigma$ ranges of limits in the absence of a signal.

[3] Y. A. Golfand and E. P. Likhtman, *Extension of the Algebra of Poincare Group Generators and Violation of p Invariance*, JETP Lett. **13** (1971) 323–326. [Pisma Zh.Eksp.Teor.Fiz.13:452-455,1971].

[4] A. Neveu and J. H. Schwarz, *Factorizable dual model of pions*, Nucl. Phys. **B31** (1971) 86–112.

[5] A. Neveu and J. H. Schwarz, *Quark Model of Dual Pions*, Phys. Rev. **D4** (1971) 1109–1111.

[6] J. Gervais and B. Sakita, *Field theory interpretation of supergauges in dual models*, Nucl. Phys. **B34** (1971) 632–639.

[7] D. V. Volkov and V. P. Akulov, *Is the Neutrino a Goldstone Particle?*, Phys. Lett. **B46** (1973) 109–110.

[8] J. Wess and B. Zumino, *A Lagrangian Model Invariant Under Supergauge Transformations*, Phys. Lett. **B49** (1974) 52.

[9] J. Wess and B. Zumino, *Supergauge Transformations in Four-Dimensions*, Nucl. Phys. **B70** (1974) 39–50.

[10] ATLAS Collaboration, *Search for a supersymmetric partner to the top quark in final states with jets and missing transverse momentum at* $\sqrt{s} = 7$ *TeV with the ATLAS detector*, Phys.Rev.Lett. **109** (2012) 211802, arXiv:1208.1447 [hep-ex].

[11] ATLAS Collaboration, *Search for direct top squark pair production in final states with one isolated lepton, jets, and missing transverse momentum in* $\sqrt{s} = 7$ *TeV pp collisions using 4.7* fb^{-1} *of ATLAS data*, Phys.Rev.Lett. **109** (2012) 211803, arXiv:1208.2590 [hep-ex].

[12] ATLAS Collaboration, *Search for a heavy top-quark partner in final states with two leptons with the ATLAS detector at the LHC*, JHEP **1211** (2012) 094, arXiv:1209.4186 [hep-ex].

[13] ATLAS Collaboration, *Search for direct production of the top squark in the all-hadronic* $t\bar{t}$+$E_{\mathrm{T}}^{\mathrm{miss}}$ *final state in 21* fb^{-1} *of pp collisions at* $\sqrt{s} = 8$ *TeV with the ATLAS detector*, ATLAS-CONF-2013-024, 2013.

[14] ATLAS Collaboration, *Search for direct top squark pair production in final states with one isolated lepton, jets, and missing transverse momentum in* $\sqrt{s} = 8$ *TeV pp collisions using 21.0* fb^{-1} *of ATLAS data*, ATLAS-CONF-2013-037, 2013.

[15] ATLAS Collaboration, *Search for direct top squark pair production in final states with two leptons in* $\sqrt{s} = 8$ *TeV pp collisions using 20* fb^{-1} *of ATLAS data*, ATLAS-CONF-2013-048, 2013.

[16] ATLAS Collaboration, *Search for direct third generation squark pair production in final states with missing transverse momentum and two b-jets in* $\sqrt{s} = 8$ *TeV pp collisions with the ATLAS detector*, ATLAS-CONF-2013-053, 2013.

[17] ATLAS Collaboration, *Search for New Phenomena in Monojet plus Missing Transverse Momentum Final States using 10/fb of pp Collisions at* $\sqrt{s} = 8$ *TeV with the ATLAS detector at the LHC*, ATLAS-CONF-2012-147, 2012.

[18] CDF Collaboration, T. Aaltonen et al., *Search for Scalar Top Quark Production in* $p\bar{p}$ *Collisions at* $\sqrt{s} = 1.96$ *TeV*, JHEP **1210** (2012) 158, arXiv:1203.4171 [hep-ex].

[19] D0 Collaboration, V. Abazov et al., *Search for scalar top quarks in the acoplanar charm jets and missing transverse energy final state in* $p\bar{p}$ *collisions at* $\sqrt{s} = 1.96$*-TeV*, Phys.Lett. **B665** (2008) 1–8, arXiv:0803.2263 [hep-ex].

[20] ATLAS Collaboration, *The ATLAS Simulation Infrastructure*, Eur. Phys. J. **C70** (2010) 823–874.

[21] GEANT4 Collaboration, S. Agostinelli et al., *GEANT4: A simulation toolkit*, Nucl. Instrum. Meth. **A506** (2003) 250–303.

[22] ATLAS Collaboration, *The simulation principle and performance of the ATLAS fast calorimeter simulation FastCaloSim*, Tech. Rep. ATL-PHYS-PUB-2010-013, CERN, Geneva, Dec, 2010.

[23] T. Gleisberg et al., *Event generation with Sherpa 1.1*, JHEP **02** (2009) 007, 0811.4622 [hep-ph].

[24] M. L. Mangano, M. Moretti, F. Piccinini, R. Pittau, and A. Polosa, *ALPGEN, a generator for hard multiparton processes in hadronic collisions*, JHEP **07** (2003) 001, arXiv:hep-ph/0206293.

[25] S. Frixione, P. Nason, and G. Ridolf, *A Positive-Weight Next-to-Leading-Order Monte Carlo for Heavy Flavour Hadroproduction*, JHEP **0709** (2007) 126, arXiv:hep-ph/0707.3088.

[26] S. Frixione and B. R. Webber, *Matching NLO QCD computations and parton shower simulations*, JHEP **0206** (2002) 029, arXiv:hep-ph/0204244 [hep-ph].

[27] B. P. Kersevan and E. Richter-Was, *The Monte Carlo event generator AcerMC version 1.0 with interfaces to PYTHIA 6.2 and HERWIG 6.3*, Comput.Phys.Commun. **149** (2003) 142, arXiv:hep-ph/0201302 [hep-ph].

[28] J. Alwall, S. Hoche, F. Krauss, N. Lavesson, L. Lonnblad, et al., *Comparative study of various algorithms for the merging of parton showers and matrix elements in hadronic collisions*, Eur. Phys. J. **C53** (2008) 473, arXiv:0706.2569 [hep-ph].

[29] G. Corcella et al., *HERWIG 6: An event generator for hadron emission reactions with interfering gluons (including supersymmetric processes)*, JHEP **01** (2001) 010, arXiv:hep-ph/0011363.

[30] T. Sjostrand, S. Mrenna, and P. Z. Skands, *PYTHIA 6.4 Physics and Manual*, JHEP **0605** (2006) 026, arXiv:hep-ph/0603175 [hep-ph].

[31] T. Sjostrand, S. Mrenna, and P. Skands, *PYTHIA 8.1*, Comput. Phys. Comm. **178** (2008) 852.

[32] J. Butterworth, J. R. Forshaw, and M. Seymour, *Multiparton interactions in photoproduction at HERA*, Z.Phys. **C72** (1996) 637–646, arXiv:hep-ph/9601371 [hep-ph].

[33] S. Catani and M. Grazzini, *DYNNLO*, Phys. Rev. Lett. **98** (2007) 222002.

[34] S. Catani et al., *DYNNLO*, Phys. Rev. Lett. **103** (2009) 082001.

[35] A. Martin et al., *Parton distributions for the LHC*, Eur. Phys. J. C **63** (2009) 189–285, arXiv:hep-ph/0901.0002.

[36] M. Aliev et al., *HATHOR HAdronic Top and Heavy quarks cross section calculatoR*, Comput. Phys. Comm. **182** (2011) 1034–1046, arXiv:hep-ph/1007.1327.

[37] A. Martin et al., *Uncertainties on alpha_s in global PDF analyses and implications for predicted hadronic cross sections*, Eur. Phys. J. C **64** (2009) 653–680, arXiv:hep-ph/0905.3531.

[38] M. Cacciari et al., *Top-pair production at hadron colliders with next-to-next-to-leading logarithmic soft-gluon resummatio*, arXiv:hep-ph/1111.5869.

[39] M. Czakon and A. Mitov, *Top++: A Program for the Calculation of the Top-Pair Cross-Section at Hadron Colliders*, arXiv:1112.5675 [hep-ph].

[40] S. Jung, H. Murayama, A. Pierce, and J. D. Wells, *Top quark forward-backward asymmetry from new t-channel physics*, Phys.Rev. **D81** (2010) 015004, arXiv:0907.4112 [hep-ph].

[41] N. Kidonakis, *Next-to-next-to-leading-order collinear and soft gluon corrections for t-channel single top quark production*, Phys.Rev. **D83** (2011) 091503, arXiv:1103.2792 [hep-ph].

[42] N. Kidonakis, *Two-loop soft anomalous dimensions for single top quark associated production with a W- or H-*, Phys.Rev. **D82** (2010) 054018, arXiv:1005.4451 [hep-ph].

[43] A. Lazopoulos, T. McElmurry, K. Melnikov, and F. Petriello, *Next-to-leading order QCD corrections to $t\bar{t}Z$ production at the LHC*, Phys. Lett. **B666** (2008) 62, arXiv:0804.2220 [hep-ph].

[44] J. M. Campbell, R. K. Ellis, and C. Williams, *Vector boson pair production at the LHC*, JHEP **1107** (2011) 018, arXiv:1105.0020 [hep-ph].

[45] W. Beenakker, M. Kramer, T. Plehn, M. Spira, and P. M. Zerwas, *Stop production at hadron colliders*, Nucl. Phys. **B515** (1998) 3–14, hep-ph/9710451.

[46] W. Beenakker, S. Brensing, M. Kramer, A. Kulesza, E. Laenen, and I. Niessen, *Supersymmetric top and bottom squark production at hadron colliders*, JHEP. **1008** (2010) 098, arXiv:1006.4771 [hep-ph].

[47] W. Beenakker, S. Brensing, M. Kramer, A. Kulesza, E. Laenen, et al., *Squark and gluino hadroproduction*, Int.J.Mod.Phys. **A26** (2011) 2637–2664, arXiv:1105.1110 [hep-ph].

[48] M. Kramer, A. Kulesza, R. van der Leeuw, M. Mangano, S. Padhi, et al., *Supersymmetry production cross sections in pp collisions at* $\sqrt{s} = 7$ *TeV*, arXiv:1206.2892 [hep-ph].

[49] M. Cacciari, G. P. Salam, and G. Soyez, *The anti-k_t jet clustering algorithm*, JHEP **04** (2008) 063, arXiv:0802.1189 [hep-ph].

[50] ATLAS Collaboration, *Jet energy measurement with the ATLAS detector in proton-proton collisions at* $\sqrt{s} = 7$ *TeV*, Eur.Phys.J. **C73** (2013) 2304, arXiv:1112.6426 [hep-ex].

[51] ATLAS Collaboration, *Performance of Missing Transverse Momentum Reconstruction in Proton-Proton Collisions at 7 TeV with ATLAS*, Eur.Phys.J. **C72** (2012) 1844, arXiv:1108.5602 [hep-ex].

[52] ATLAS Collaboration, *Electron performance measurements with the ATLAS detector using the 2010 LHC proton-proton collision data*, Eur.Phys.J. **C72** (2012) 1909, arXiv:1110.3174 [hep-ex].

[53] ATLAS Collaboration, *Muon Momentum Resolution in First Pass Reconstruction of pp Collision Data Recorded by ATLAS in 2010*, ATLAS-CONF-2011-046, 2011.

[54] ATLAS Collaboration, *A measurement of the muon reconstruction efficiency in 2010 ATLAS data using J/psi decays*, ATLAS-CONF-2012-125, 2012.

[55] ATLAS Collaboration, *Muon reconstruction efficiency in reprocessed 2010 LHC proton-proton collision data recorded with the ATLAS detector*, ATLAS-CONF-2011-063, 2011.

[56] ATLAS Collaboration, *b-jet tagging calibration on c-jets containing D∗ mesons*, ATLAS-CONF-2012-039, 2012.

[57] ATLAS Collaboration, *Measurement of the b-tag Efficiency in a Sample of Jets Containing Muons with 5 fb*^{1} *of Data from the ATLAS Detector*, ATLAS-CONF-2012-043, 2012.

[58] ATLAS Collaboration, *Measurement of the Mistag Rate of b-tagging algorithms with 5 fb*$^{-1}$ *of Data Collected by the ATLAS Detector*, ATLAS-CONF-2012-040, 2012.

[59] ATLAS Collaboration, *Improved luminosity determination in pp collisions at* $\sqrt{s} = 7$ *TeV using the ATLAS detector at the LHC*, arXiv:1302.4393 [hep-ex].

[60] ATLAS Collaboration, *Performance of the ATLAS Trigger System in 2010*, Eur.Phys.J. **C72** (2012) 1849, arXiv:1110.1530 [hep-ex].

[61] ATLAS Collaboration, *Performance of primary vertex reconstruction in proton-proton collisions at* $\sqrt{s} = 7$ *TeV in the ATLAS experiment*, ATLAS-CONF-2010-069 (2010) .

[62] ATLAS Collaboration, *Selection of jets produced in proton-proton collisions with the ATLAS detector using 2011 data*, ATLAS-CONF-2012-020 (2012) .

[63] ATLAS Collaboration, *Further search for supersymmetry at* $\sqrt{s} = 7$ *TeV in final states with jets, missing transverse momentum and isolated leptons with the ATLAS detector*, Phys.Rev. **D86** (2012) 092002, arXiv:1208.4688 [hep-ex].

[64] ATLAS Collaboration, *Search for squarks and gluinos with the ATLAS detector in final states with jets and missing transverse momentum using 4.7* fb^{-1} *of* $\sqrt{s} = 7$ *TeV proton-proton collision data*, Phys.Rev. **D87** (2013) 012008, arXiv:1208.0949 [hep-ex].

[65] G. Cowan, K. Cranmer, E. Gross, and O. Vitells, *Asymptotic formulae for likelihood-based tests of new physics*, Eur. Phys. J. **C71** (2011) 1554, arXiv:1007.1727 [physics.data-an].

[66] A. L. Read, *Presentation of search results: The CL(s) technique*, J. Phys. G **G28** (2002) 2693–2704.

[67] LEP Collaboration, *LEPSUSYWG/04-01.1, http://lepsusy.web.cern.ch/lepsusy/*, 2004.

A Cut flow tables

Cut	$m_{\tilde{t}} = 200\,\text{GeV}$, $m_{\tilde{\chi}_1^0} = 125\,\text{GeV}$		$m_{\tilde{t}} = 200\,\text{GeV}$, $m_{\tilde{\chi}_1^0} = 195\,\text{GeV}$	
All	376397	100%	376397	100%
Generator filter	181996	48.2%	103073	27.3%
		Preselection		
Jet quality requirements	180960	48.0%	102416	27.2%
Trigger	122776	32.6%	73988	19.6%
$E_{\text{T}}^{\text{miss}} > 150$ GeV	30202	9.1%	34031	9.0%
leading jet p_{T}>150 GeV	17960	4.8%	20206	5.4%
$\text{N}_{\text{jets}} \leq 3$	10527	2.8%	18091	4.8%
$\Delta\phi(\text{jet}, \mathbf{p}_{\text{T}}^{\text{miss}}) > 0.4$	8760	2.3%	17027	4.5%
Lepton vetoes	8728	2.3%	17009	4.5%
		M1		
$E_{\text{T}}^{\text{miss}} > 220$ GeV	2976	0.8%	8785	2.3%
leading jet p_{T}>280 GeV	1182	0.3%	3457	0.9%

Table 7: Cut flow for two SUSY signal points with $m_{\tilde{t}} = 200\,\text{GeV}$ and $m_{\tilde{\chi}_1^0} = 125\,\text{GeV}$ (moderate Δm) and $m_{\tilde{\chi}_1^0} = 195\,\text{GeV}$ (small Δm) for the monojet-like selection. The signal sample is produced using `MadGraph` 5 version 1.3.33 with the CTEQ6L1 PDF set and `Pythia` 6.426 with the AUET2B tune. MLM matching is used with up to one additional jet in the `MadGraph` matrix element, a `MadGraph` k_{T} measure of 25 GeV, and a `Pythia` jet measure cut off of 25 GeV.

Cut	$m_{\tilde{t}} = 200\,\text{GeV}$, $m_{\tilde{\chi}_1^0} = 125\,\text{GeV}$		$m_{\tilde{t}} = 200\,\text{GeV}$, $m_{\tilde{\chi}_1^0} = 195\,\text{GeV}$	
All	376397	100%	376397	100%
Generator filter	181996	48.2%	103073	27.3%
		Preselection		
Jet quality requirements	181755	48.2%	102935	27.3%
Trigger	124009	32.9%	74397	19.7%
$E_{\text{T}}^{\text{miss}} > 150\,\text{GeV}$	35240	9.34%	34502	9.15%
leading jet $p_{\text{T}} > 150\,\text{GeV}$	20225	5.36%	22606	5.99%
$N_{\text{jets}} \geq 4$	14418	3.82%	6085	1.61%
$\Delta\phi(\text{jet}, \mathbf{p}_{\text{T}}^{\text{miss}}) > 0.4$	10905	2.89%	5126	1.36%
Lepton vetoes	10876	2.88%	5122	1.36%
		C1		
$E_{\text{T}}^{\text{miss}} > 410\,\text{GeV}$	314	0.08%	705	0.19%
leading jet $p_{\text{T}} > 270\,\text{GeV}$	284	0.08%	591	0.16%
c-tagging	20.8	0.006%	9.12	0.004%

Table 8: Cut flow for two signal points with $m_{\tilde{t}} = 200\,\text{GeV}$ and $m_{\tilde{\chi}_1^0} = 125\,\text{GeV}$ (moderate Δm) and $m_{\tilde{\chi}_1^0} = 195\,\text{GeV}$ (small Δm) for the charm-tagged selection. The signal sample is produced using `MadGraph` 5 version 1.3.33 with the CTEQ6L1 PDF set and `Pythia` 6.426 with the AUET2B tune. MLM matching is used with up to one additional jet in the `MadGraph` matrix element, a `MadGraph` k_{T} measure of 25 GeV, and a `Pythia` jet measure cut off of 25 GeV.

B Auxiliary plots for the monojet-like analysis

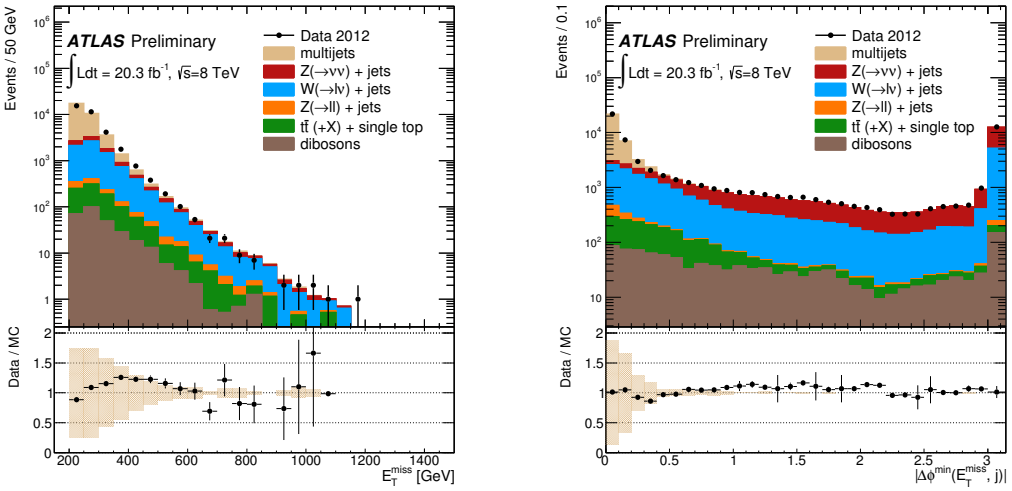

Figure 10: Distribution of $E_{\mathrm{T}}^{\mathrm{miss}}$ and the min($\Delta\phi$(jet,$\mathbf{p}_{\mathrm{T}}^{\mathrm{miss}}$)). Events with $E_{\mathrm{T}}^{\mathrm{miss}}$ larger than 220 GeV, leading jet p_{T} larger than 280 GeV and 3 or less jets are plotted. The region $\Delta\phi < 0.4$ is used for the multijet normalization.

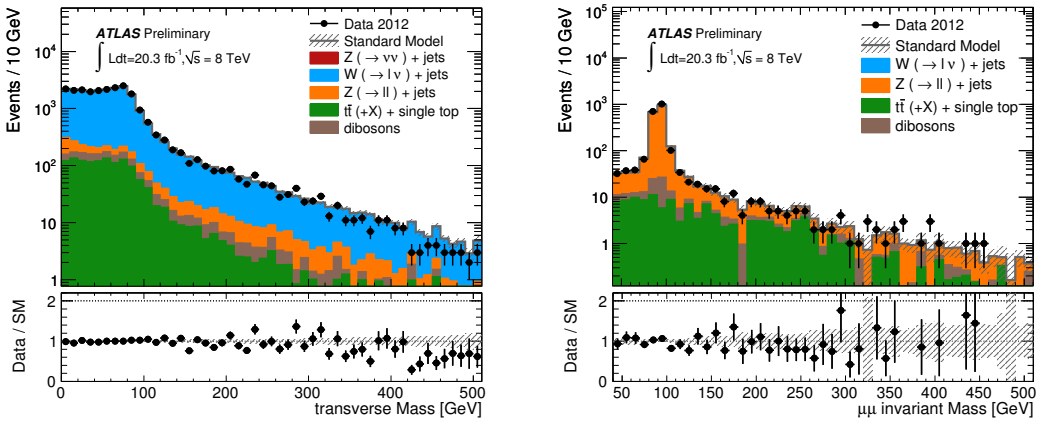

Figure 11: Distribution of the transverse mass (in the $W(\rightarrow \mu\nu)$ control region) and the di-muon invariant mass (in the Z/γ^{*} ($\rightarrow \mu^{+}\mu^{-}$) control region) for the monojet-like analysis.

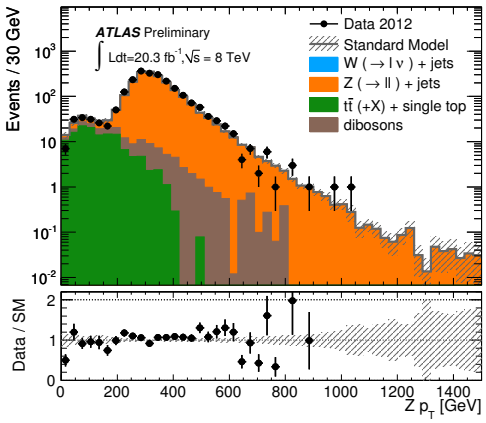

Figure 12: Distribution of the Z boson p_{T} in the Z/γ^* ($\rightarrow \ \mu^+ \ \mu^-$) control region for the monojet-like analysis.

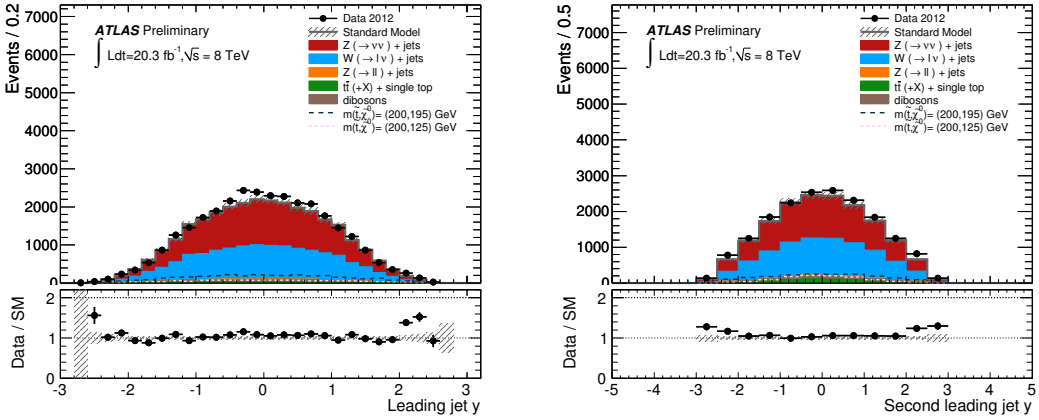

Figure 13: Distribution of the rapidity for the leading and second jet in the M1 signal region.

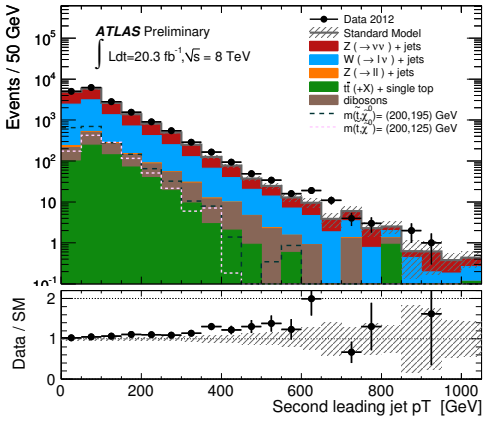

Figure 14: Distribution of the second jet p_{T} in the M1 signal region.

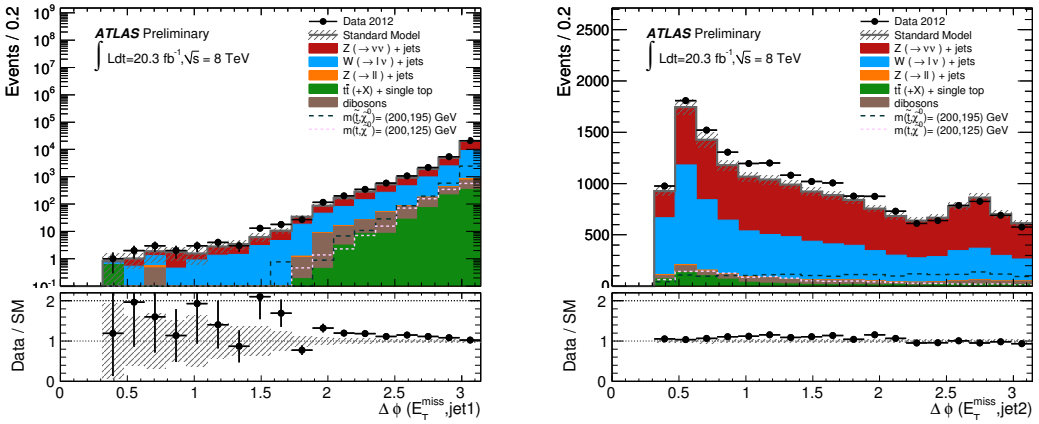

Figure 15: Distribution of $\Delta\phi(E_{\mathrm{T}}^{\mathrm{miss}}, \mathrm{jet})$ for the first and second jet in the M1 signal region.

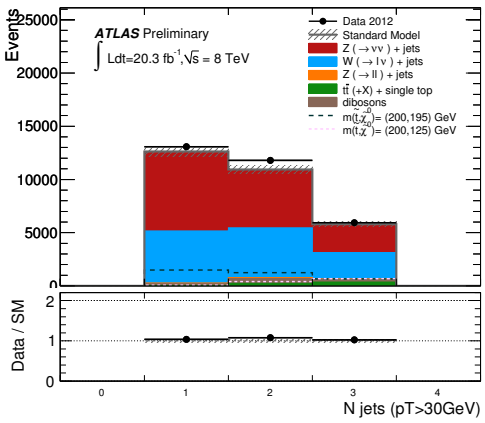

Figure 16: Distribution of the jet multiplicity in the M1 signal region.

C Auxiliary plots for the charm-tagged analysis

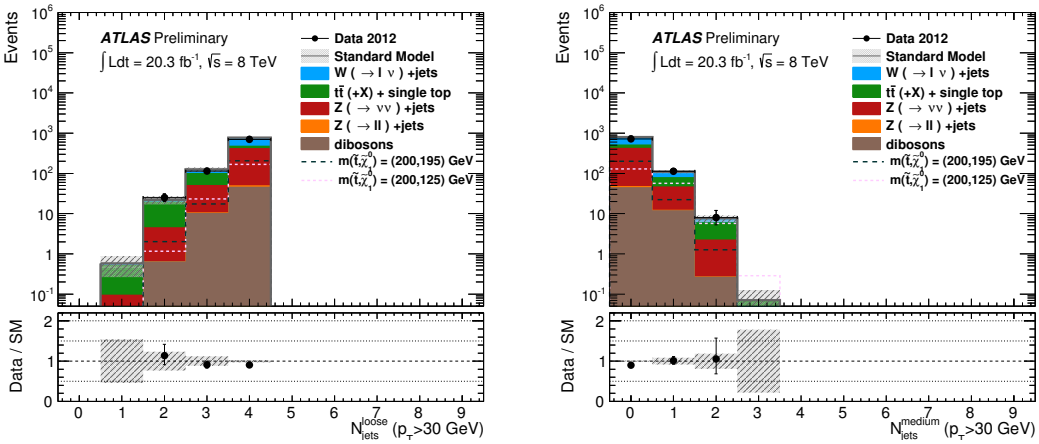

Figure 17: Distribution of the number of loose tagged (left) and medium tagged (right) jets among the four leading jets in the charm tagged signal region before applying the tagging requirements.

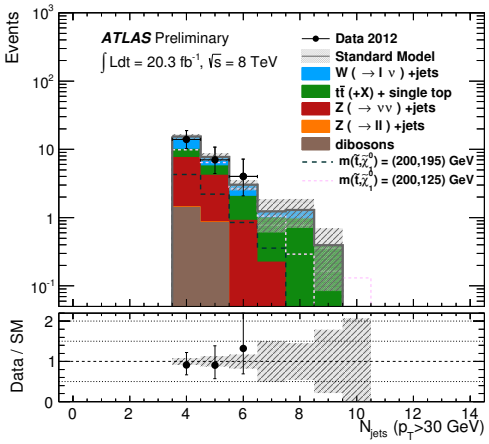

Figure 18: Distribution of the number of jets in the charm tagged signal region.

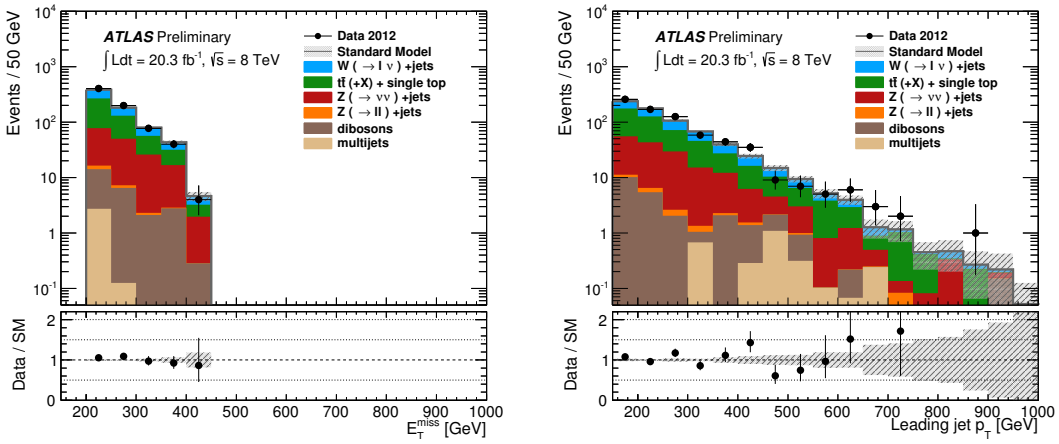

Figure 19: Distribution of the missing transverse energy (left) and leading jet transverse momentum (right) for validation region V2 after the fit, see Table 4.

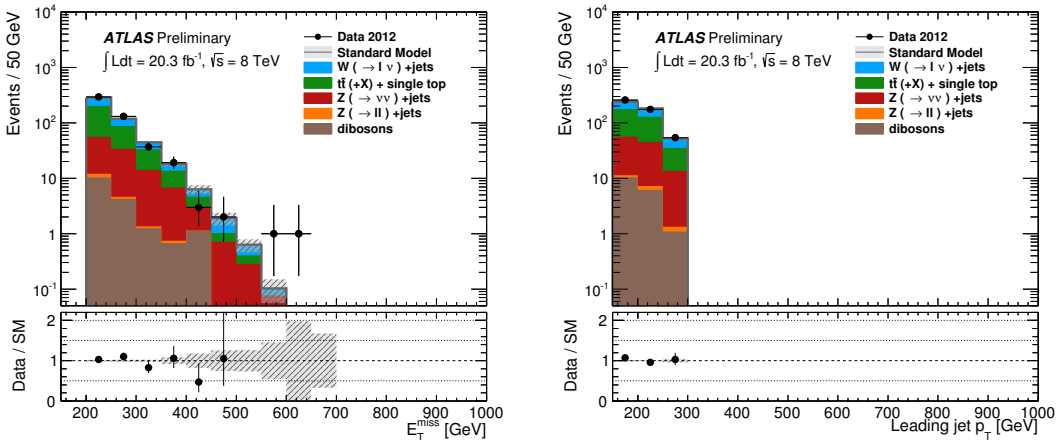

Figure 20: Distribution of the missing transverse energy (left) and leading jet transverse momentum (right) for validation region V3 after the fit, see Table 4.

D Exclusion limits for the monojet-like and charm-tagged analyses

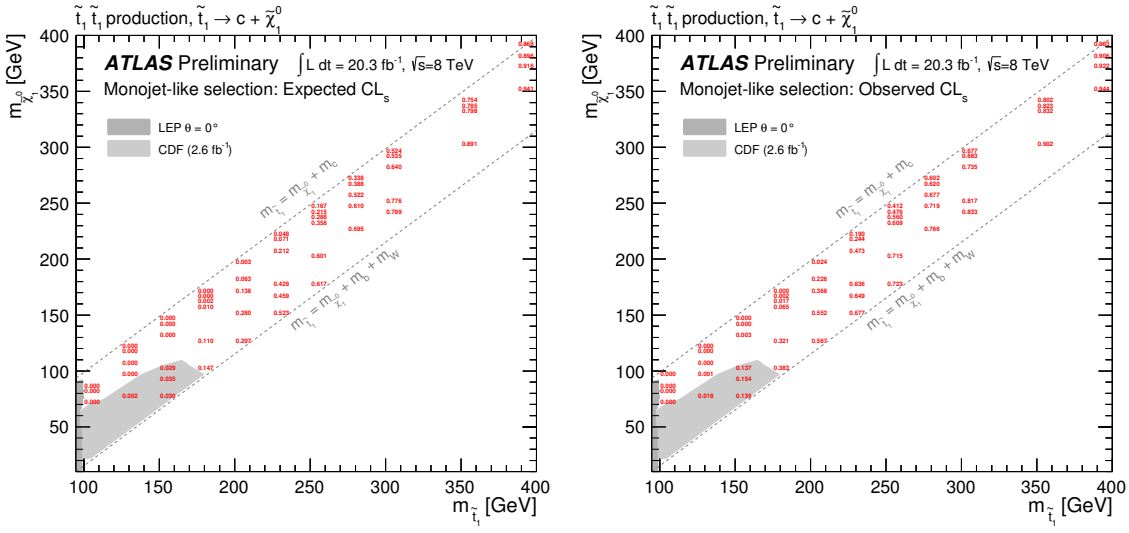

Figure 21: Expected (left) and observed (right) CLs for the monojet-like analysis M1.

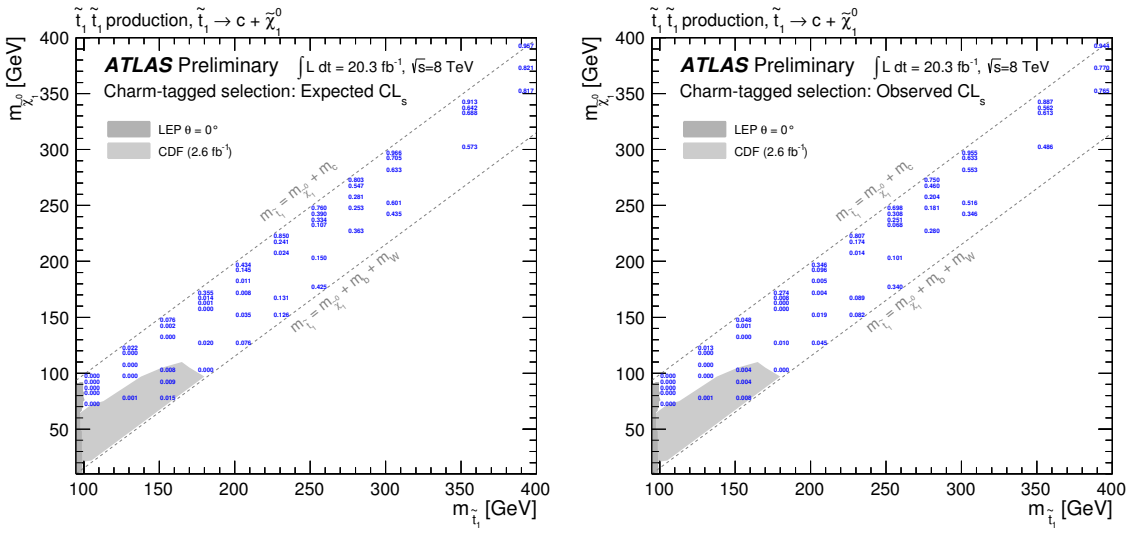

Figure 22: Expected (left) and observed (right) CLs for the *c*-tagged analysis C1.

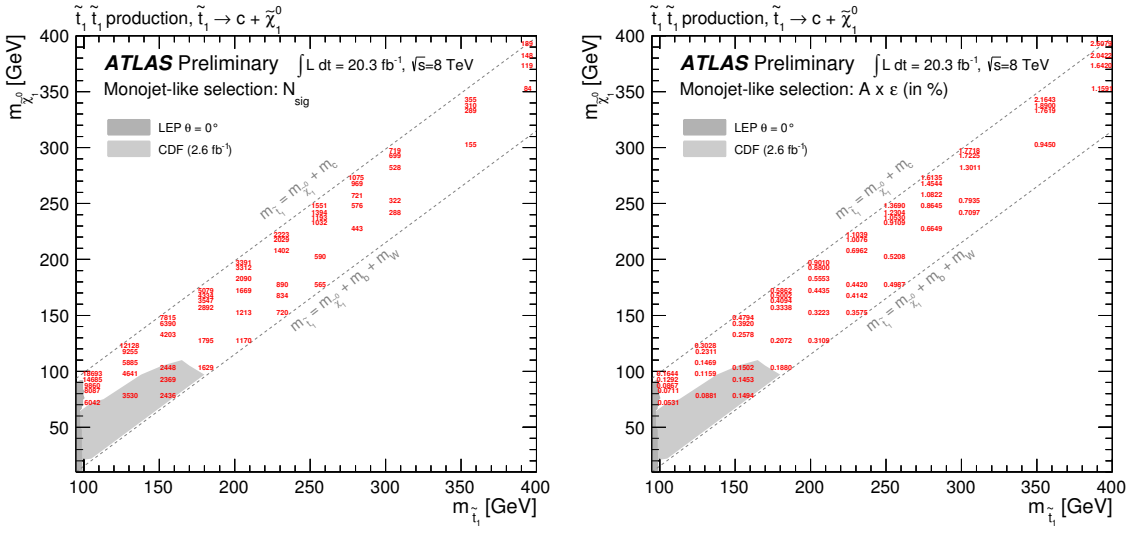

Figure 23: Number of expected signal events (left) and signal acceptance times efficiency (right) for the monojet-like analysis M1.

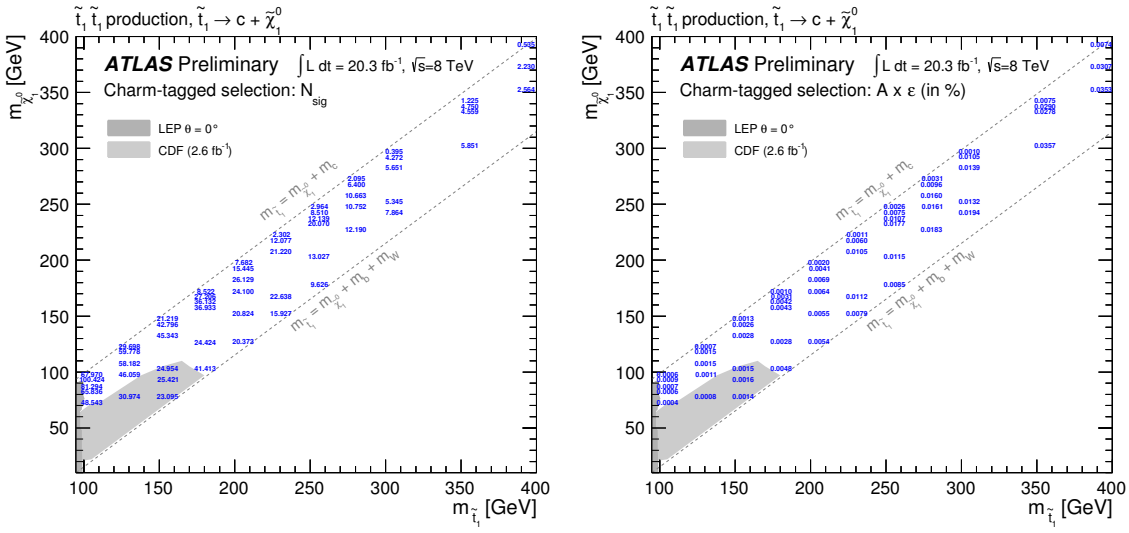

Figure 24: Number of expected signal events (left) and signal acceptance times efficiency (right) for the *c*-tagged analysis C1.

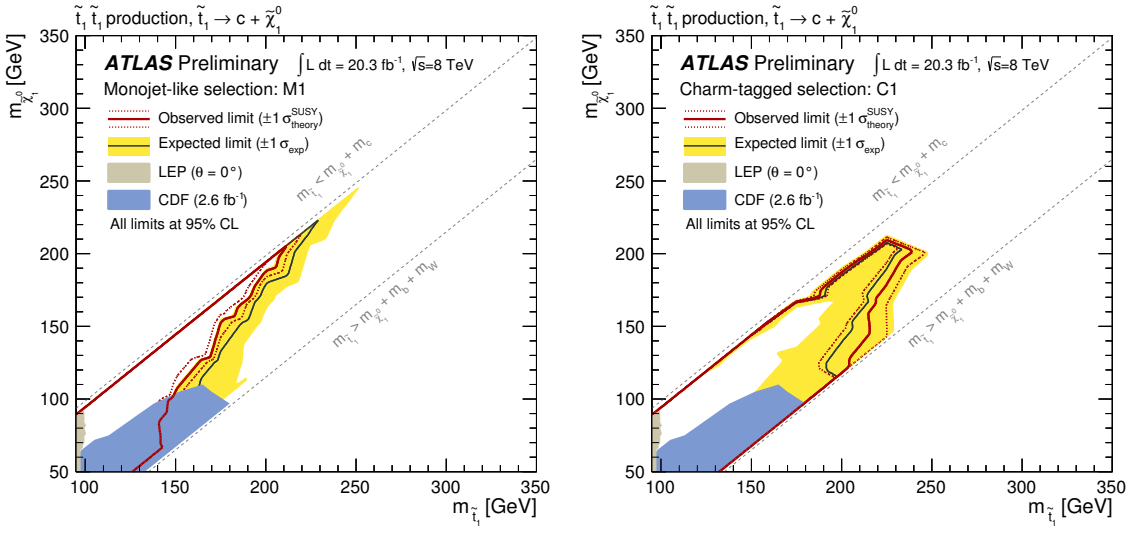

Figure 25: Exclusion plane at 95% CL. as a function of stop and neutralino masses for the monojet-like (M1, left) and c-tagged (C1, right) analysis. The observed (red line) and expected (black line) upper limits from this analysis are compared to previous results from Tevatron experiments, and from LEP experiments at CERN with squark mixing angle θ^o. The dotted lines around the observed limit indicate the range of observed limits corresponding to $\pm1\sigma$ variations on the NLO SUSY cross section predictions. The shaded area around the expected limit indicates the expected $\pm1\sigma$ ranges of limits in the absence of a signal.

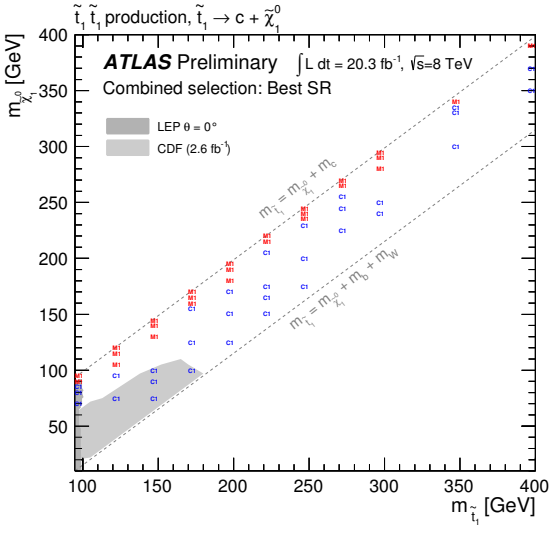

Figure 26: Analysis selected for every signal point (M1, C1 as defined in Section 4) based on best expected CLs.

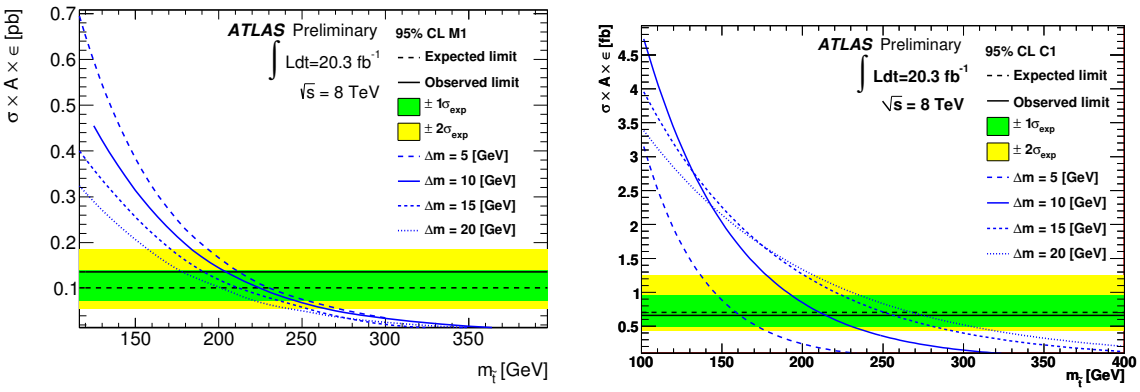

Figure 27: Observed and expected 95% CL limits on the visible cross section for the monojet-like (left) and c-tagged selection (right) compared to the stop predictions as a function of stop mass for different Δm.

E Event display

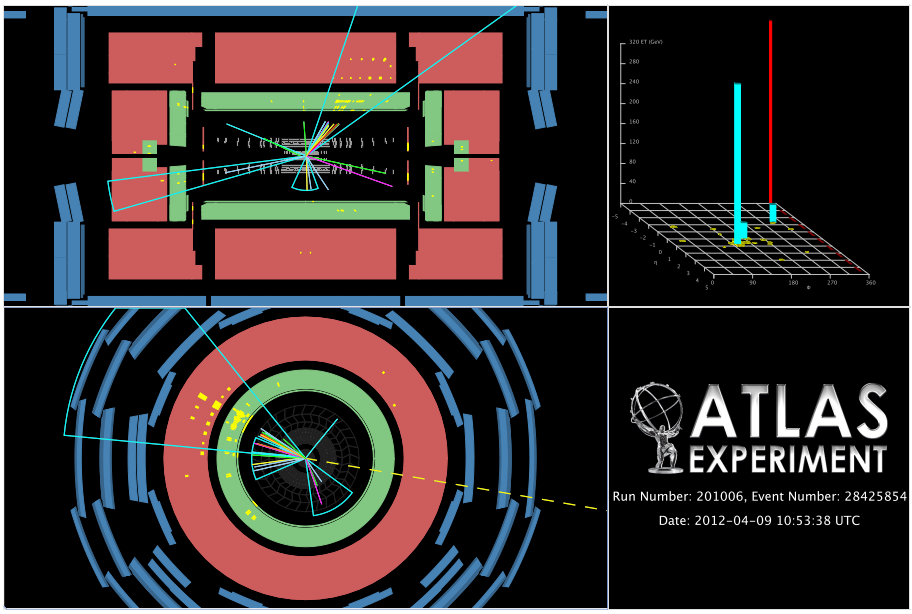

Figure 28: Event display of an event with $E_{\mathrm{T}}^{\mathrm{miss}} = 359$ GeV, and three jets in the final state with (p_{T}, η) of (314 GeV, 0.74), (37 GeV, -2.4), and (31 GeV, -0.03), respectively. Only charged tracks with $p_{\mathrm{T}} > 2.5$ GeV and clusters in the electromagnetic (hadronic) calorimeter with $E_{\mathrm{T}} > 0.5$ GeV ($E_{\mathrm{T}} > 1.0$ GeV) are displayed.